C_3N_5: A Low Bandgap Semiconductor Containing an Azo-linked Carbon Nitride Framework for Photocatalytic, Photovoltaic and Adsorbent Applications

Pawan Kumar,[1]* Ehsan Vahidzadeh,[1] Ujwal K. Thakur,[1] Piyush Kar,[1] Kazi M. Alam,[1] Ankur Goswami,[1] Najia Mahdi,[1] Kai Cui,[2] Guy M. Bernard,[3] Vladimir K. Michaelis[3] and Karthik Shankar[1]*

[1] *Department of Electrical and Computer Engineering, University of Alberta, 9211 - 116 St, Edmonton, Alberta, Canada T6G 1H9*

[2] *Nanotechnology Research Centre, National Research Council of Canada, Edmonton, Canada T6G 2M9*

[3] *Department of Chemistry, University of Alberta, Edmonton, Alberta, Canada, T6G 2G2*

*Email: Pawan Kumar (pawan@ualberta.ca); Karthik Shankar (kshankar@ualberta.ca)

Abstract

Modification of carbon nitride based polymeric 2D materials for tailoring their optical, electronic and chemical properties for various applications has gained significant interest. The present report demonstrates the synthesis of a novel modified carbon nitride framework with a remarkable 3:5 C:N stoichiometry (C_3N_5) and an electronic bandgap of 1.76 eV, by thermal deammoniation of melem hydrazine precursor. Characterization revealed that in C_3N_5 polymer, two *s*-heptazine units are bridged together with azo linkage, which constitutes an entirely new and different bonding fashion from g-C_3N_4 where three heptazine units are linked together with tertiary nitrogen. Extended conjugation due to overlap of azo nitrogens and increased electron density on heptazine nucleus due to the aromatic π network of heptazine units lead to an upward shift of the valence band maximum resulting in bandgap reduction down to 1.76 eV. XRD, He-ion imaging, HR-TEM, EELS, PL, fluorescence lifetime imaging, Raman, FTIR, TGA, KPFM *etc* clearly show that the properties of C_3N_5 are distinct from pristine carbon nitride (g-C_3N_4). When used as an electron transport layer (ETL) in $MAPbBr_3$ based halide perovskite solar cells, C_3N_5 outperformed g-C_3N_4, in particular generating an open circuit photovoltage as high as 1.3 V, while C_3N_5 blended with $MA_xFA_{1-x}Pb(I_{0.85}Br_{0.15})_3$ perovskite active layer achieved a photoconversion efficiency (PCE) up to 16.7 %. C_3N_5 was also shown to be an effective visible light sensitizer for TiO_2 photoanodes in photoelectrochemical water splitting. Due to its electron-rich character, the C_3N_5 material displayed instantaneous adsorption of methylene blue from aqueous solution reaching complete equilibrium within 10 min, which is significantly faster than pristine g-C_3N_4 and other carbon-based materials. C_3N_5 coupled with plasmonic silver nanocubes promotes plasmon-exciton co-induced surface catalytic reactions reaching completion at much low laser intensity (1.0 mW) than g-C_3N_4 which showed sluggish performance even at high laser power (10.0 mW). The relatively narrow bandgap and 2D structure of C_3N_5 make it an interesting air-stable and temperature-resistant semiconductor for optoelectronic applications while its electron-rich character and intra-sheet cavity make it an attractive supramolecular adsorbent for environmental applications.

KEYWORDS: carbon nitride, melem, *s*-heptazine, dye adsorption, photocatalysis, water spilitting, solar cells, plasmonic photocatalysis.

1. Introduction

The last few decades have witnessed the rise of semiconducting, all-organic polymers as excellent metal-free and visible light-active materials for various optoelectronic and energy harvesting applications.[1] Although impressive improvements in performance have been achieved, particularly for plastic solar cells, the synthesis procedures for semiconducting polymers are cumbersome and difficult to scale up,[2] and the organic semiconductors themselves are unstable under the action of heat, light and/or ambient air.[3] Consequently, there are scalability concerns related to semiconducting polymers,[4] and requirement of heavy encapsulation to achieve even modest durability in the photovoltaic application. The same concerns, related to oxidative stability and durability, have also ruled out the use of semiconducting polymers in photocatalytic applications.

A very different approach toward forming and exploiting all-organic, polymeric semiconductors in optoelectronic and energy harvesting applications consists of using doped and substituted graphenic frameworks as building blocks to achieve two-dimensional (2D) semiconductors with well-defined bandgaps and structural motifs.[5, 5-6] The major advantages of graphenic semiconductors are their chemical robustness and the simplicity of synthesis. Several graphenic semiconductors are synthesizable using solvothermal synthesis and/or solid-state reactions, and graphenic semiconductors are perfectly stable in ambient conditions up to temperatures of several hundred degrees Celsius. As a result of this exceptional stability, almost no structural or chemical degradation of photocatalytic action is observed even after several re-use cycles.[7]

Among graphenic semiconductors, graphitic carbon nitride (g-C_3N_4), composed of tris-*s*-triazine (*s*-heptazine, C_6N_7) units bridged together with nitrogen atoms to give a 2D graphitic structure has gained significant interest due to its astonishing electronic, optical, and physicochemical properties.[8] Continuous repetition of the heptazine motif leads to a bandgap of 2.7 eV with band edge positions (E_{CB}, −1.1 eV and E_{VB}, +1.6 eV) that render it compatible with sunlight-driven water splitting, CO_2 photoreduction and the photooxidation of a number of organic compounds.[9] Further, the plentiful presence of electron rich sites and basic nitrogens in the g-C_3N_4 scaffold enables the promotion of various catalytic reactions *i.e.* alkylation, esterification, oxidation, *etc* and pollutant removal (dye adsorption). [6a, 10] The somewhat wide bandgap of g-C_3N_4 means that it can absorb only the ultraviolet and blue fraction of solar spectrum ($\lambda < 450$ nm) which limits its performance in photocatalytic and photovoltaic applications. Doping with various heteroatoms such as P, F, B, and S has been utilized to improve the visible light absorption profile and photoefficiency.[11] Like all semiconductors, g-C_3N_4 suffers the innate drawback of carrier recombination detrimental to catalytic and photocatalytic processes. Many surface modification approaches such as increasing the surface area *via* soft and hard templating, using two or more precursors, transformation of bulk material into sheets, doping with metals (Ag, Cu, Rh, Pt, Na, *etc*) and metal oxides (CoO_x) for electron and hole capture, coupling with other semiconductors/metal complexes to form heterojunctions, and blending with graphene have been employed to improve the photocatalytic and catalytic performance of g-C_3N_4.[12] However, less attention has been paid to chemical structure modification which can lead to the generation of a more robust, band edge tuned g-C_3N_4 framework with entirely new physicochemical properties for efficient catalytic/photocatalytic applications. It has been found that addition of extra nitrogen-rich moieties in the g-C_3N_4 scaffold to increase the N:C ratio from 4:3 ratio in CN can reduce the bandgap significantly, due to a more extended conjugated network and the participation of the lone pair on the N atom with the π conjugated system of heptazine motif. Vinu et al. demonstrated the synthesis of N-rich carbon nitride (MCN-8) using 3-amino-1,2,4-triazole to afford C_3N_5 stoichiometry resulting in a significant decrease in bandgap (2.2 eV) due to extended conjugation.[13] However, this increase in N:C ratio to 5:3 (from the 4:3 ratio in g-C_3N_4) was due to the presence of the N-rich 1,2,4-triazole moiety linked to the heptazine motif and not because of the direct incorporation of the extra N atom in the heptazine nucleus. The same group has also reported the synthesis of mono/and diamino-s-tetrazine based carbon nitride materials (i.e. MCN-ATN, MCN-4, and MCN-9) with C_3N_5 to C_3N_6 stoichiometry using 3-amino-1,2,4-triazine/aminoguanidine hydrochloride precursor and SBA-15/KIT-6 templating material.[14] The N rich 1,2,4-triazine or 1,2,4,5-tetrazine moieties were bridged together with tertiary nitrogen in a similar fashion to triazine-based carbon nitride and a significant decrease in band gap was observed due to the addition of extra nitrogens. In a recent report, mesoporous triazole and triazine framework modified carbon nitride materials with $C_3N_{4.8}$ empirical formula synthesized by using 5-amino-1H-tetrazole (5-ATTZ) precursor and their hybrid with graphene displayed excellent performance in the oxygen reduction reaction.[15] Fang et al. reported the synthesis of nitrogen self-doped graphitic carbon nitride (C_3N_{4+x}) by heating hydrazine treated melamine in a sealed ampoule. In C_3N_{4+x}, the excess N atoms replace terminal C atoms in the heptazine nucleus and the excess charge on the N atom gets redistributed leading to electron rich heptazine motifs due to which C_3N_{4+x} possessed a narrower bandgap (2.65 eV) with concomitant shifts in the conduction and valence band edge positions (E_{CB}, –0.98 eV and E_{VB}, +1.67 eV).[16] In these N rich carbon nitrides, the N rich triazine or heptazine based unit remains linked together with tertiary nitrogen, $N(C)_3$ and increased stochiometric N:C ratio was due to the replacement of C *via* N in triazine or heptazine ring system. Similarly, carbon-rich C_3N_4 network also facilitates bandgap narrowing and efficient charge separation due to the extended conjugated network. Zhang et al. reported the hydrothermal synthesis of low bandgap, C rich C_3N_4 materials with extended conjugated networks using melamine (as heptazine ring source) and glucose (as carbon source) precursors.[12c, 17] However, the use of melamine and other C and N sources can afford only C_3N_4 structures possessing randomly distributed domains within the C_3N_4 framework due to the uncontrolled reaction and these regions work as trap centers. Melem (2,5,8-triamino-*s*-heptazine) considered the smallest monomeric unit of g-C_3N_4 framework, provides the opportunity to manipulate chemical structure by incorporating other units in the C_3N_4 framework in a more controlled fashion.[16-18] Shiraishi *et al.* reported the synthesis of modified CN-polydiimide framework (g-C_3N_4/PDI_x) by solid-state reaction between melem and electron deficient pyromellitic dianhydride (PMDA) and demonstrated that the band edge positions of g-C_3N_4/PDI_x could be tuned by limiting the number of PDI units in the framework.[19] Heterostructured (C_{ring}-C_3N_4) embodiments of conductive, in-plane, π conjugated carbon rings incorporated in the C_3N_4 matrix were prepared by thermal dehydrogenation reaction between glucose and melem, and the obtained C_{ring}-C_3N_4 heterostructure achieved fast spatial charge transfer from g-C_3N_4 to C_{ring} motif facilitating efficient water splitting.[18d, 20] The replacement of amino functionalities on melem/melamine by nitrogen-rich functionalities *i.e.* azide ($-N_3$) expedited the synthesis of N-rich carbon nitride *i.e.* 2,5,8-triazido-*s*-heptazine, $(C_6N_7)(N_3)_3$ which after thermal heating, afforded N-rich carbon nitride.[20-21] Likewise, triazine containing N-rich CN was also synthesized by thermal annealing of 2,4,6-triazido-1,3,5-triazine [cyanuric triazide, $(C_3N_3)(N_3)_3$].[20, 22] However, the synthesis procedure involved sodium azide and concomitant shock sensitive explosion hazards; furthermore, azide intermediates are highly undesirable.

Herein, we demonstrated the synthesis of novel modified carbon nitride framework with a C_3N_5 stoichiometry by thermal deammoniation of 2,5,8-trihydrazino-s-heptazine, also known as melem hydrazine (MH), as a safe and environmentally benign precursor (Figure 1). The obtained carbon nitride modified framework was denoted as C_3N_5 due to its 3:5 C:N stoichiometric ratio. Characterization studies revealed that the C_3N_5 framework contains heptazine moieties bridged together by azo linkage (–N=N–). The presence of azo linkage extends the π conjugated network due to overlap between the *p* orbitals on N atoms constituting the azo bond and π system of heptazine motif which resulted in the reduction of the electronic bandgap to 1.76 eV. C_3N_5 displayed improved photosensitization properties at longer wavelengths for solar water splitting. Further, due to the increased electron charge density on the ring nitrogen, C_3N_5 exhibited instantaneous adsorption of methylene blue from aqueous solution. Solar cell devices fabricated using low bandgap C_3N_5, as an electron transporting layer (ETL) in $MAPbBr_3$ based perovskite solar cells demonstrated improved power conversion efficiency (PCE), open circuit voltage (V_{oc}) *etc*. compared to solar cells made from g-C_3N_4 based ETL due to tuned band alignment. Blending a small amount of C_3N_5 (4.0 wt%) with $MA_xFA_{1-x}Pb(I_{0.85}Br_{0.15})_3$ perovskite active layer led to an increase in PCE up to 16.68% with V_{oc} of 1.065V and J_{sc} of 22.87 mA/cm^2 higher than conventional and g-C_3N_4 blended solar cell architectures. Compared to g-C_3N_4, C_3N_5 exhibited a remarkably enhanced performance in the plasmon-exciton co-driven photoreduction of 4-nitrobenezenethiol to 4,4'-dimercaptoazobenzene.

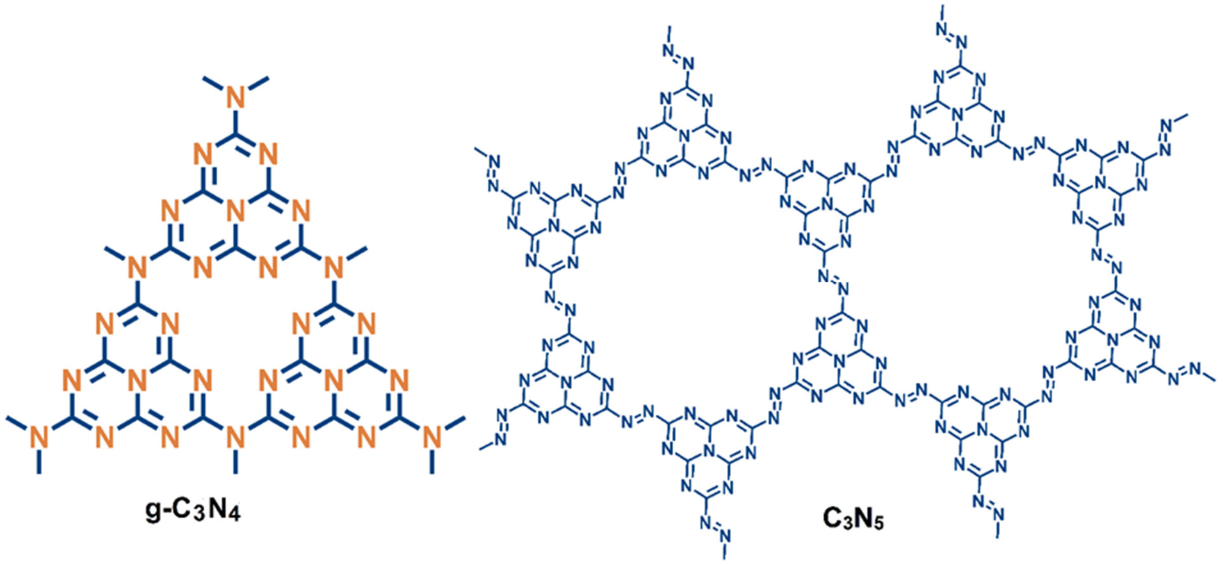

Figure 1. Chemical structure of g-C_3N_4 and carbon nitride modified C_3N_5 framework.

2. Results and discussion

Melem (2,5,8-triamino-*s*-heptazine) served as the precursor monomeric unit for the synthesis of C_3N_5 polymer. Melem was synthesized by heating melamine at 425 ºC overnight followed by purification in boiling water. The obtained melem was treated with hydrazine hydrate ($NH_2NH_2.H_2O$, 55% in water) in an autoclave at 140 ºC for 24 h. The treatment of melem with hydrazine hydrate transformed amino ($–NH_2$) functionalities into hydrazino ($–NH–NH_2$) functionalities which afforded melem hydrazine, MH (2,5,8-trihydrazino-*s*-heptazine).[23] The obtained white melem hydrazine was subjected to programmed heating at 450 ºC for 2 h to obtain orange colored C_3N_5 polymer (Figure 2) (See supporting information for experimental details). Melem hydrazine has a highly hydrogen bonded structure which facilitates the formation of an azo-bridged heptazine framework by thermal condensation. Previously, Gillan also reported the formation of similar azo-bridged functionalities by heating nitrogen-rich 2,4,6- cyanuric triazide or triazido-1,3,5-triazine $(C_3N_3)(N_3)_3$ to form differential composition triazine-based carbon nitride.[22, 24] In the same report Gillan suggested that transformation of cyanuric triazide into azo-bridged triazine carbon nitride framework proceeded through the nitrene intermediate ($C_3(N_3)_2N$:) and that the formation of C_3N_5 from melem hydrazine might proceed *via* a similar intermediate due to the thermolabile nature of hydrazine functionalities. The structures of melem, melem hydrazine and hydrogen bonded melem hydrazine are given in supporting information (Figure S1).

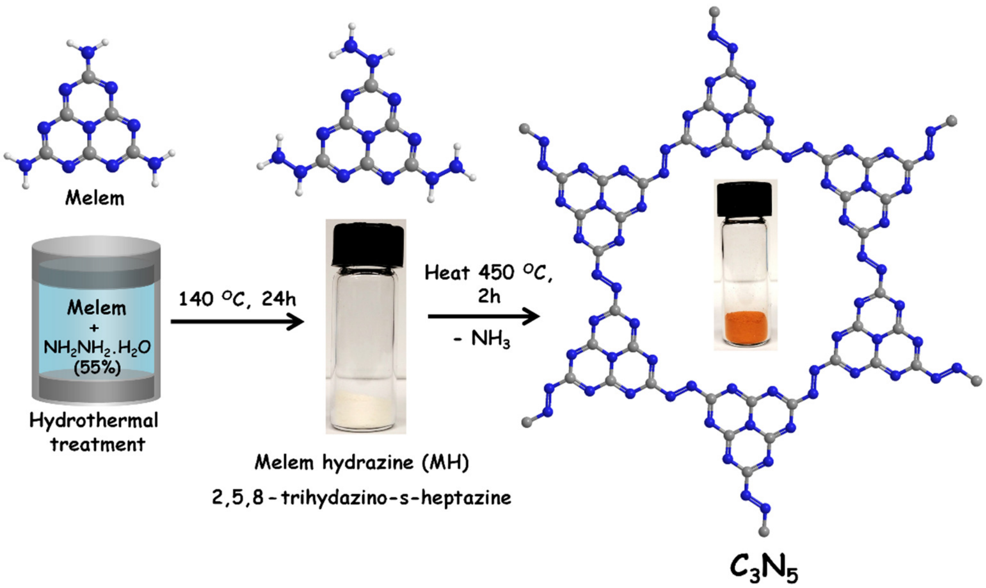

Figure 2. Synthesis schematic of C_3N_5 from melem *via* melem hydrazine (Atom color: N - blue, C - gray and H - white). The vials show the distinct color of the reaction product contrasted with that of the precursor.

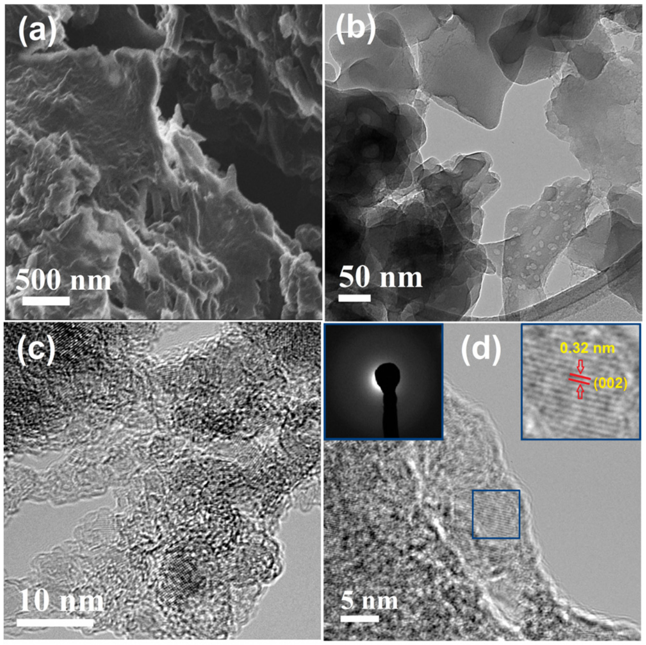

Figure 3. (a) He-ion image of C_3N_5, and HR-TEM images of C_3N_5 (b) at 50 nm, (c) at 10 nm and (d) at 5 nm scale bar; left and right insets showing SAED diffraction pattern and interplanar *d* spacing, respectively.

The surface morphology of the C_3N_5 polymer was investigated using a He-ion microscope equipped with an electron flood gun to facilitate positive charge neutralization accumulated from the He-ion beam (Figure 3a). The He-ion images of MHP show a rough, crumpled graphenic scaffold with some erupted morphologies which indicate that the high temperature treatment of MH monomeric unit facilitated polymerization into an irregular sheet-like structure. The fine structure of C_3N_5 material was determined using high resolution transmission electron microscopy (HR-TEM) (Figure 3b-d). The carbon nitride like layered sheet architecture is clearly evident in the TEM image of C_3N_5 at 50 nm scale bar (Figure 3b). Under long duration exposure of the electron beam, C_3N_5 starts to degrade and shrink which likely resulted due to high energy electrons breaking the –N=N– linkage. HR-TEM images at 10 nm and 5 nm scale bar show crystallite fringes of nanoporous multilayered sheets with an interplanar *d*-spacing of 0.32 nm, corresponding to the 002 plane of the graphitic structure (Figure 3c, 3d, and inset). The observed *d*-spacing in C_3N_5 was identical to g-C_3N_4 from which we infer that during the thermal polymerization step, the stacking pattern of sheets in C_3N_5 remains similar to that in bulk g-C_3N_4. The broad, less intense ring in the selected area electron diffraction (SAED) pattern was attributed due to diffraction of electrons by the 002 plane; however, the low intensity of the ring suggests amorphous nature of the material (inset of Figure 3d).

The surface chemical composition of the synthesized material was investigated using X-ray photoelectron spectroscopy, XPS (Figure 4). The XPS elemental survey scan of C_3N_5 shows peaks corresponding to C1s, N1s, Na1s, Cl2p, and O1s (Figure S2a). The presence of Na1s and Cl2p is due to intercalated Na^+ ions in the supramolecular cavity of the polymeric motif (Figure 1) and the residual NaCl formed during the purification step of MH. After excluding Na1s, Cl2p and O1s peaks, the at% of C and N in the C_3N_5 were found to be 36.76 % and 63.24 % respectively, which represent an empirical formula of $C_3N_{5.16}$ for the C_3N_5 polymer (Table 1). The obtained composition matched well with theoretical C_3N_5 (N-62.50 at% and C-37.50 at%) stoichiometric carbon nitride materials. The high resolution XPS spectrum of C_3N_5 in C1s region was deconvolved into two peak components at binding energies of 284.8 eV and 287.9 eV corresponding to the presence of sp^3 and sp^2 hybridized carbons, respectively (Figure 4a). The sp^3 carbon peak originated from adventitious carbons, edge group carbons and turbostratic carbons present in the scaffold of C_3N_5 polymer while the relatively stronger sp^2 peak appeared due to N=C–N type aromatic carbons which constitute the carbon nitride like framework of C_3N_5. [25] The core level HR-XPS in N1s after deconvolution gave two peak components located at 398.7 eV and 400.2 eV. The peak at a binding energy of 398.7 eV was assigned to tertiary $N–(C)_3$ and secondary C=N–C nitrogens present in the aromatic ring structure while another peak at 400.2 eV was due to the presence of primary residual $–NH_2$ and bridging C–N=N–C type nitrogens (Figure 4b). [25-26] From the N1s XPS spectrum, the at % of N present in aromatic ring (N_{ring}) and bridging ($N_{bridging}$) were found to 60.47 % and 39.53 % respectively and the at% ratio obtained was 3:2, which strongly supports the proposed structure in which two heptazine units are interconnected with the azo (–N=N–) motif and is also consistent with the theoretical C_3N_5 azo linked structure (Table 1). Furthermore, HR-XPS in Na1s region gave a peak at 1071.9 eV due to the presence of Na^+ ions in the polymeric skeleton and residual NaCl (Figure S2b). The two peak components in Cl2p XPS, at binding energy values of 198.7 eV and 200.2 eV ascribed to $Cl2p_{3/2}$ and $Cl2p_{1/2}$ further validated the presence of Cl^- in the form of NaCl (Figure S2c). Two XPS peaks in the O1s region located at 531.6 eV and 532.4 eV were associated with surface adsorbed adventitious oxygens and –OH groups (Figure S2d). The nature of C and N bonding in g-C_3N_4 and C_3N_5 was elucidated with electron energy loss spectroscopy (EELS) (Figure 4c,d and Figure S3). The normalized EELS spectra of g-C_3N_4 and C_3N_5 exhibited two major symmetric peaks due to contribution of C-K and N-K edge loss. The C K-edges signal of both g-C_3N_4 and C_3N_5 was composed of two peaks located at located at 284.6 and 293.2 eV corroborated to 1s-π* and 1s-σ* electronic transition of sp^2 hybridized carbons trigonally coordinated with nitrogens in *s*-heptazine nucleus (Figure 4c).[14a, b, 27] The relative intensity of π* C K-edge signal and π*/σ* peak area ratio of C_3N_5 was higher than g-C_3N_4 suggesting increased conjugation in C_3N_5 due to extended π orbitals overlap between bridging azo functionalities and heptazine motifs.[28] The formation of extended π conjugated network in C_3N_5 was also supported by increased UV-Vis absorption profile and shorter TRPL lifetime decay (Figure 7 and 8). The N K-edges energy loss peaks for g-C_3N_4 and C_3N_5 located at 399.8 and 408.5 eV, assigned to 1s-π* and 1s-σ* electronic transition of sp^2 hybridized nitrogens in heptazine ring and bridging N, further verify sp^2 hybridized nitrogen-rich carbon nitride framework (Figure 4d).[13] Absence of any new peak in N K-edge loss of C_3N_5 demonstrate bridging nitrogens in C_3N_5 have almost identical electronic environment like $N(C)_3$ nitrogens in g-C_3N_4.[29] The relative peak intensity of N K-edge π* signal of C_3N_5 was slightly lower than g-C_3N_4 demonstrating enhanced contribution of azo motifs in 1s-σ* transition The replacement of tertiary bridging nitrogens, $N(C)_3$ in g-C_3N_4 *via* azo nitrogens, C-N=N-C render lone pair on azo nitrogens which contribute to σ* signal and relative intensity of π* signal was suppressed. However, total peak area of N K-edge peak for C_3N_5 was increased which demonstrate addition of extra nitrogens in carbon nitride framework. The N:C atomic ratio of C_3N_5 was calculated to be 1.62 which was in close agreement with theoretical value (1.66) and C:N value obtained from CHNS analysis (1.65). Slightly lower N content might be due to cleavage of azo bond resulting in loss of some nitrogens under high energy electron beam.

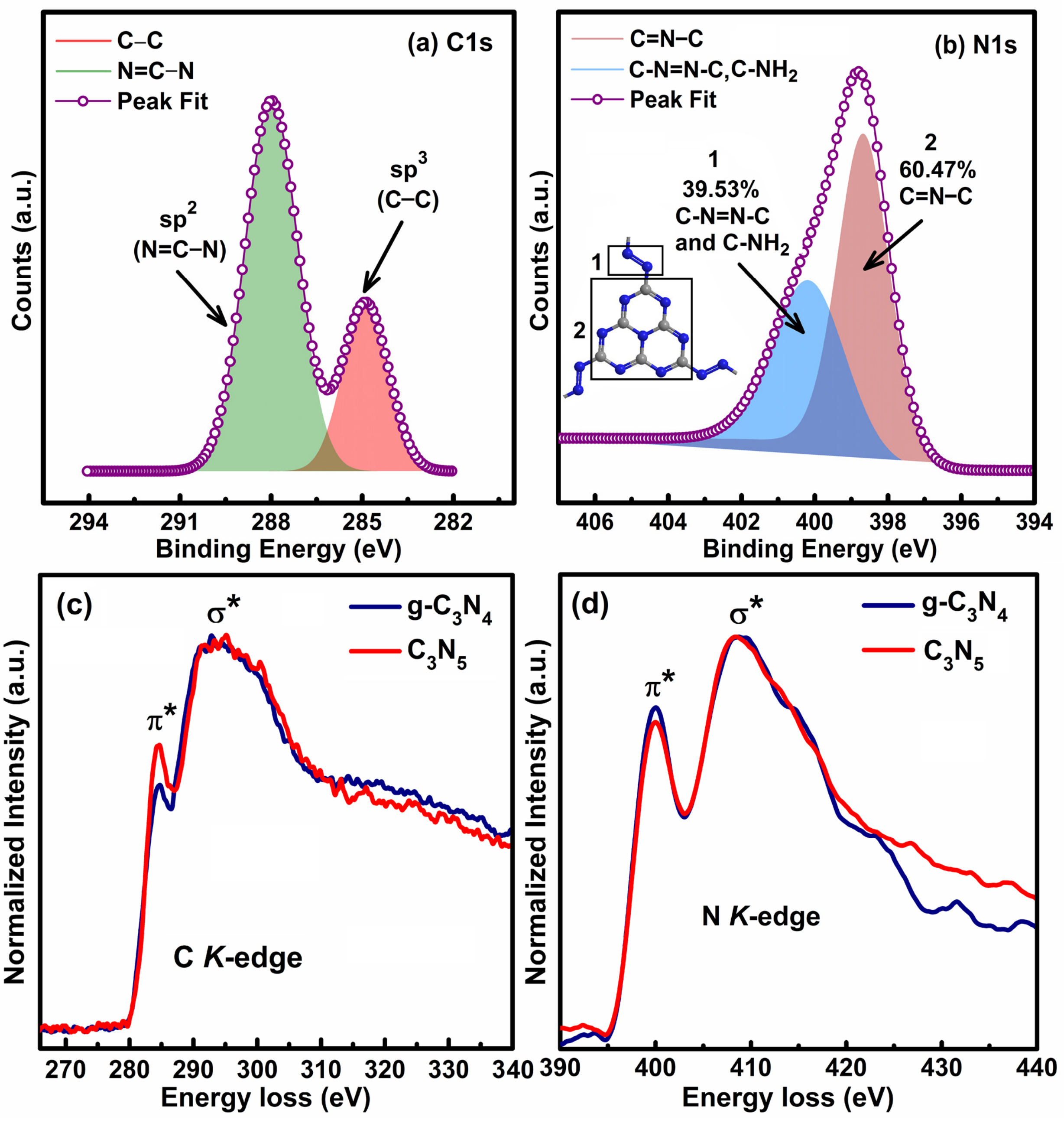

Figure 4. The core level HR-XPS spectra of C_3N_5 in (a) C1s region, (b) N1s region and normalized EELS spectra of g-C_3N_4 and C_3N_5 showing relative intensity of π* and σ* peaks for (c) C K-edge and (d) N K-edge loss.

Table 1. (a) Elemental analysis of C_3N_5 showing C, H, and N wt% and empirical formula and (b) XPS elemental analysis of C_3N_5 showing at% and empirical formula and their comparison with theoretical C_3N_5 composition.

(a) Elemental analysis						
Serial. No.		**N (wt%)**	**C (wt%)**	**H (wt%)**	**Empirical formula**	**N_{ring}:$N_{bridging}$ (at% ratio)**
1.	CHN analysis	61.27	31.81	2.68	$C_3N_{4.95}H_{1.01}$	-
2	Theoretical wt% value	66.02	33.98	-	C_3N_5	3:2 (60:40)
(b) XPS elemental analysis						
		N (at%)	**C (at%)**	**H (at%)**	Empirical formula	**N_{ring}:$N_{bridging}$ (at% ratio)**
3.	XPS analysis	63.24	36.76	-	$C_3N_{5.16}$	~ 3:2 (60.47:39.53)
4.	Theoretical at% value	62.50	37.50	-	C_3N_5	3:2 (60:40)

To probe the proposed composition and structure of the synthesized C_3N_5 material, CHNS elemental analysis was performed which gave 61.27 wt% N, 31.81 wt% C and 2.68 wt% H suggesting an empirical formula of $C_3N_{4.95}H_{1.01}$ which was in close proximity with the theoretical wt% for C_3N_5 composition (Table 1). Slight difference between predicted and observed C:N ratio might be due to the presence of unbonded $-NH_2$ at the edge of sheets, formed by cleavage of hydrazino group ($-NH-NH_2$) at elevated temperature and loss of some azo nitrogens.[9b, 10b] As expected, sulfur was not present at measurable levels. Notably, the observed hydrogen might arise from $–NH_2$ and –OH groups present at the edge of the polymeric framework.

To elucidate the chemical structure of MH and C_3N_5 materials, solid-state nuclear magnetic resonance (NMR) spectroscopy using the cross-polarization magic-angle spinning (CPMAS) technique was performed (Figure 5). CPMAS NMR enables the structural investigation of local- and medium-range structure in micro- and nano-crystalline compounds. The ^{13}C CPMAS NMR spectra of melem hydrazine (MH) display three NMR signals at 164, 160 and 154 ppm (Figure 5a). The ^{13}C NMR signals at 164 and 160 ppm originated from N_2C–$NHNH_2$ carbons while the resonance at 154 ppm was observed from CN_3 carbons of the heptazine nucleus. The observed signals were in good agreement with the reported NMR spectra for MH and melem based structures.[18a 24, 30] The CPMAS NMR spectrum of C_3N_5 exhibits two ^{13}C NMR signals of approximately equal intensity at 164 and 156 ppm for N_2C–N=N– and CN_3 carbons (Figure 5b).[24, 30-31] The N_2C–$NHNH_2$ carbon signal of MH located at 160 ppm arising due to C–H functionalities disappeared in the ^{13}C NMR of C_3N_5, which confirms removal of –$NHNH_2$ protons and formation of an azide linkage during polymerization step agreeing with ^{15}N CPMAS NMR, *vide infra*. Furthermore, the appearance of equally intense (Cc:Ce/1:1.07) ^{13}C peaks in the ^{13}C NMR spectrum of C_3N_5 suggests that heptazine units are in the presence of a symmetric azo bridging motif (where Cc corresponds to central carbons in ring and Ce to external carbons bonded to azo N). A slight shift to higher frequency in CN_3 carbon peaks from 154 ppm in MH to 156 ppm in C_3N_5 suggests shielding of carbons due to N2p overlap of azo and aromatic π system which extends the π conjugated network.[32]

The ^{15}N CPMAS NMR spectrum of MH exhibits four signals, –207, –252, –273 and –317 ppm (Figure 5c).[23a] The ^{15}N NMR signal at –207 ppm and another weak signal at –273 ppm were assigned to (NC_2) and (NC_3) nitrogens of the heptazine motif,[23a, 31b, 32-33] while the peaks at –252 and –317 ppm assigned to NH_2 and NH terminal nitrogens of hydrazino moiety.[33-34] The transformation of MH to C_3N_5 proceeds with removal of NH_3 and formation of azo linkage which was evident from the disappearance of NH_2 and NH peaks at –252 and –317 ppm in the ^{15}N NMR spectrum of C_3N_5 (Figure 5d). The two NMR peaks in the ^{15}N NMR spectra of C_3N_5 at -197 and -248 (weak) ppm were attributed to NC_2 and NC_3 nitrogens of heptazine skeleton while another peak at –271 ppm arose from –N=N– (and residual NHs) type nitrogens. As the N atoms are in similar chemical environments, a semi-quantitative CPMAS NMR analysis of the ^{15}N peak areas achieved by peak integration of NC_2 and NC_3 and –N=N– resonances was found give a ratio of 1.00:0.18:0.54 which was in good agreement with the theoretical value (1.00:0.17:0.5) calculated for C_3N_5 polymeric structure containing heptazine units interconnected with azo linkage (Figure S1). Furthermore, ^{1}H NMR of MH gave an intense peak at 5.11 ppm due to NH and NH_2 hydrogens (Figure S4). This intense peak disappeared in the ^{1}H NMR spectra of C_3N_5 further confirming the removal of NH hydrogens and a very broad peak centered at 9.18 ppm appeared due to intercalated hydrogen, and residual carboxy and aldehyde hydrogens (essential for the CPMAS approach to function whereby ^{1}H magnetization is transferred to ^{13}C and ^{15}N). All these NMR results validate the successful synthesis of a modified carbon nitride framework.

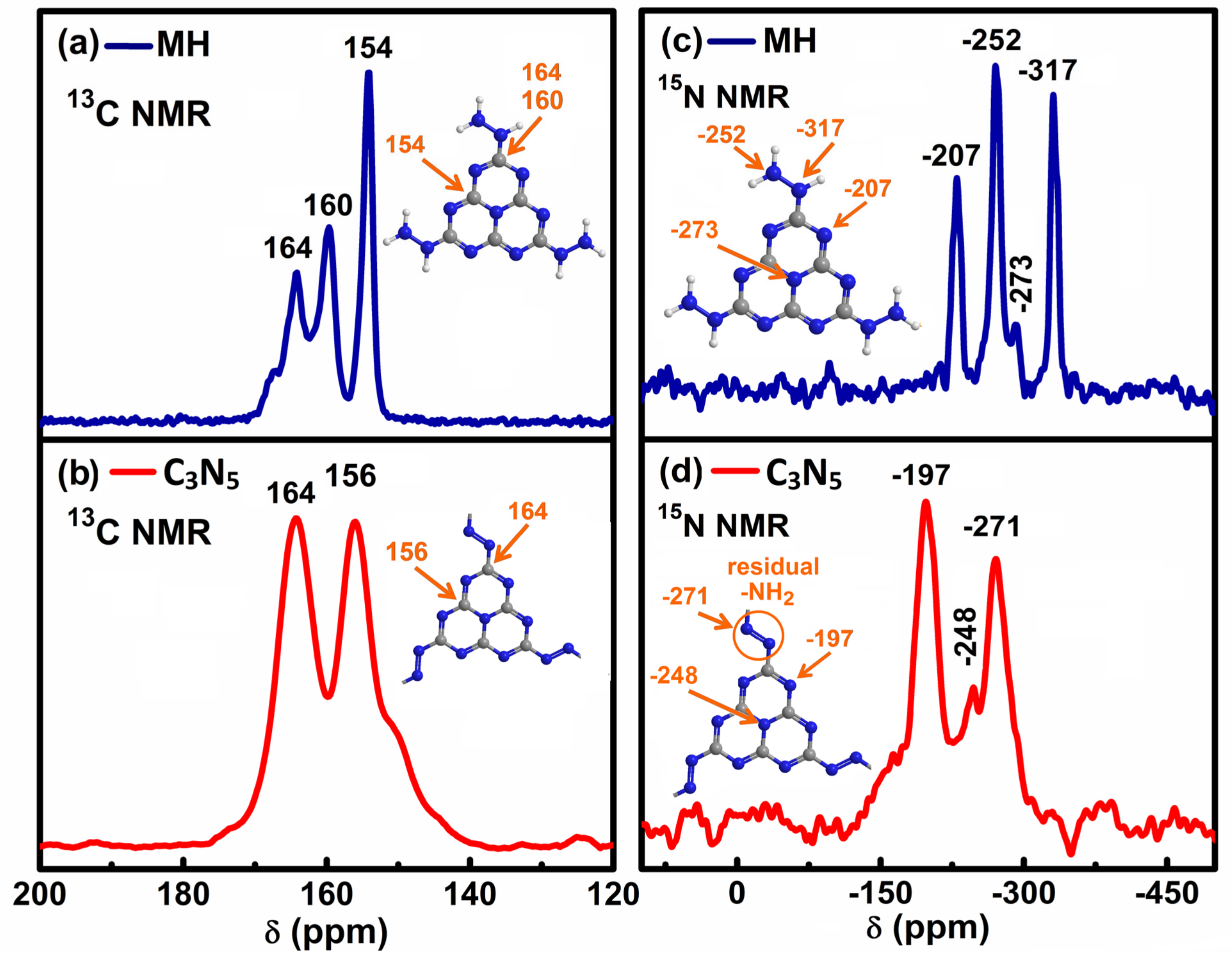

Figure 5. CPMAS NMR spectra (a) ^{13}C of MH, (b) ^{13}C of C_3N_5, (c) ^{15}N of MH and (d) ^{15}N of C_3N_5.

Fourier transform infrared (FTIR) spectroscopy was employed to determine the change in functional moiety in the material (Figure 6a-d). The FTIR spectrum of melem shows characteristic broad peaks at 3109 cm^{-1} due to the combined symmetric and antisymmetric stretch vibrations of –NH$_2$ and –OH (ν_{N-H} and ν_{O-H}) groups. The IR bands at 1595, 1411, 1230 and 1078 cm^{-1} are ascribed to the C–N stretch (ν_{C-N}) of heptazine (C_6N_7) aromatic nucleus (Figure 6a).[18a, 31b, 34a, 35] The N–H stretch band ranging from 3153–2895 cm^{-1} for MH was found to become broader due to combinational symmetric and asymmetric N–H stretches of –NH–NH$_2$ group in MH which confirms the successful transformation of $–NH_2$ moiety in melem to $–NH–NH_2$ in melem hydrazine (Figure 6b). The broadening of NH peak was attributed to strong intermolecular hydrogen bonding in MH molecules.[35-36] However, all stretching and bending peaks due to heptazine aromatic ring skeleton remain preserved which indicates that the heptazine motif remains unchanged during the hydrazine treatment. Additionally, some new peaks emerged at 1095 and 965 cm^{-1} implicating the N–N stretch and $–NH_2$ rocking vibration respectively.[18a, 36-37] Graphitic carbon nitride shows characteristic peaks at 3145 cm^{-1} due to residual $–NH_2$ and –OH stretch and 1639–1145 cm^{-1} due to triazine ring stretch and 798 cm^{-1} for triazine ring bending vibration was in good agreement with the reported literature (Figure 6c).[37-38] After conversion of MH to C_3N_5 by thermal annealing, the intensity of $–NH–NH_2$ peak of MH was diminished which implicated the transformation of $–NH–NH_2$ group into azo (–N=N–) linkage through the removal of NH_3 (Figure 6d). It is important to note that vibration of symmetrical –N=N– azo linkage is forbidden due to which no new sharp peak due to azo functionalities was observed. The possibility of –NH–NH– bond can be neglected due to the absence of any strong N–H band; however very weak broad peaks arise due to some residual $–NH_2$ present at the edge of the polymeric framework. This fact was well supported by CHNS analysis which showed the presence of only one H for each stoichiometric C_3N_5 unit (Table 1). Further, other peaks of MH at 1095 and 965 cm^{-1} due to N–N stretch and $–NH_2$ rocking vibration disappear in C_3N_5, which confirmed the transformation of hydrazine group into azo moiety. Peaks corresponding to the C_3N_4 framework at 1542, 1315 and 887 cm^{-1} were absent in C_3N_5 which suggests an entirely different network of C_3N_5 in comparison to g-C_3N_4.

The changes in phase structure and crystalline nature of melem, MH, g-C_3N_4, and C_3N_5 were investigated through the measurement of X-ray diffraction (XRD) (Figure 6). The XRD pattern of melem demonstrated a series of peaks located at 12.5º, 13.6º, 16.7º, 18.4º, 19.7º, 22.0º, 25.2º, 27.2º and 30.4º, in close agreement with previous reports (Figure 6e).[38-39] The XRD results indicate the absence of any melamine impurity in the melem sample.[18b, 39a] Due to the transformation of melem into melem hydrazine, the XRD pattern of MH changed, with new peaks being observed at 2θ values of 7.3º, 7.9º, 8.4º, 12.9º, 13.7º, 14.8º, 25.1º and 28.0º (Figure 6f). Bulk g-C_3N_4 shows two distinct XRD peaks at 2θ values of 27.1° and 13.0° indexed to the 002 and 100 planes of carbon nitride materials (Figure 6g). The 002 peak with a 0.32 nm interplanar *d* spacing was correlated to interplanar stacking of sheets while 100 peaks with a 0.68 nm spacing was specific to in-plane structural packing of heptazine units (Figure 6g).[18b, 39b, 40] The XRD pattern of C_3N_5 exhibits one broad 002 peak at 27.6º corresponded to 0.33 nm interplanar sheet distance. The slight increase in 2θ value and *d* spacing can be explained due to repulsion between electron rich π conjugated C_3N_5 sheets as in graphite (0.34 nm) (Figure 6h). Further, the absence of 100 peak – a specific feature of in-plane packing, suggests distortion in the carbon nitride framework and broadening of the nanochannel distance between heptazine units due to azo (–N=N–) bridging linkage, further consistent with ^{13}C and ^{15}N NMR resonance broadening above, suggesting local/medium-range disorder. Also, bridging of two heptazine units with two nitrogens through in-plane lattice packing is less efficient in C_3N_5 which was responsible for the absence of any expected peak at lower 2θ values. These XRD results clearly support the distinct structure of C_3N_5 possessing azo linkage.

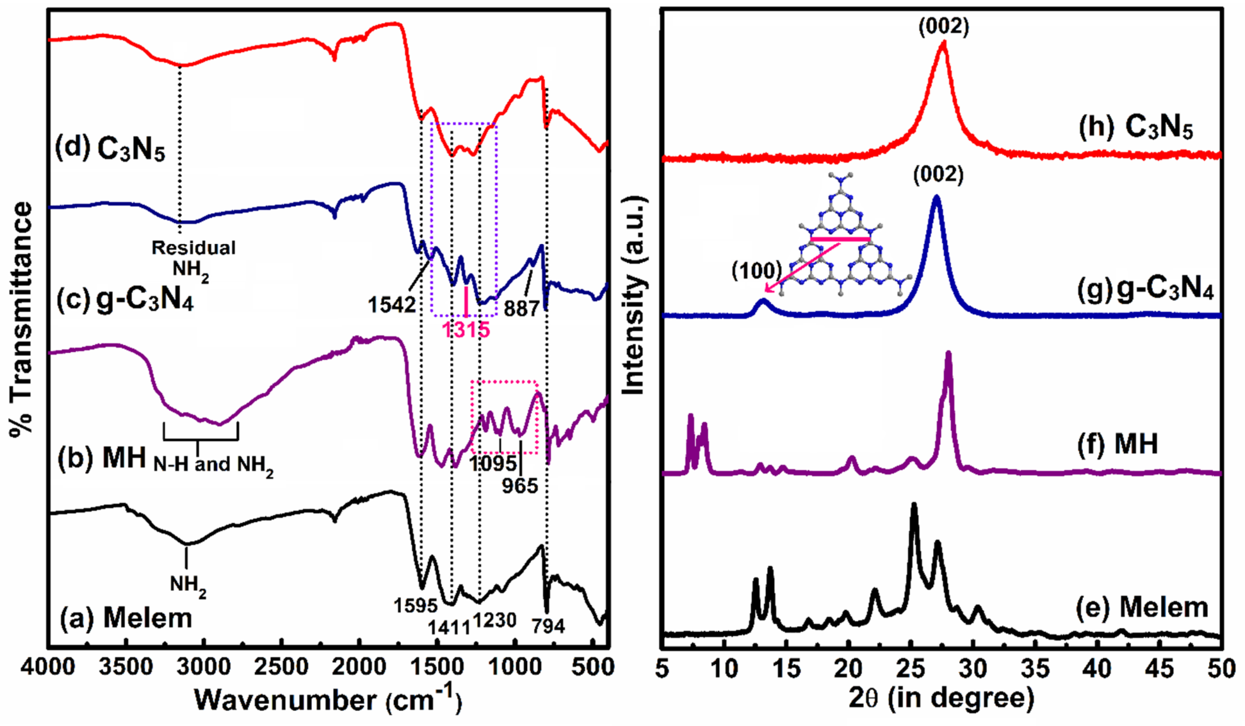

Figure 6. FTIR spectra of (a) Melem, (b) Melem hydrazine, (c) g-C_3N_4, (d) C_3N_5, and XRD diffraction pattern of (e) Melem, (f) Melem hydrazine, (g) g-C_3N_4, (h) C_3N_5.

Raman spectra of melem acquired using 632 nm laser excitation show characterstic fingerprint peaks of melem at 435 and 697 cm^{-1} due to heptazine ring (C_6N_7) breathing modes and a broad hump at 1452 cm^{-1} due to $-NH_2$ bending mode (Figure S5a).[18a, 40a] Raman spectra of MH demonstrate many signature peaks correlated to the core at 472, 744 and 1529 cm^{-1} which were shifted in comparison to melem due to functionalization while other peaks due to various vibrations of the heptazine nucleous and hydrazine group were observed at 127, 342, 537, 985, 1159, 1314 and 3071 cm^{-1}, in good agreement with the reported literature (Figure S5b).[18a, 23a, 40b, 41] The Raman spectra of g-C_3N_4 display many prominent peaks due to the heptazine framework at 471, 697, 706 cm^{-1} (heptazine ring breathing modes) and two additional peaks at 1233 and 1567 cm^{-1} corresponding to the $-NH_2$ bending mode and graphitic G band (Figure S5c).[23a, 42] Further, the presence of a broad hump extended from 1100-1600 cm^{-1} suggests multilayer stacking of g-C_3N_4 sheets.[41, 43] In the Raman spectra of C_3N_5, only trace peaks of melem hydrazine motif are observed which indicates the complete transformation of MH to C_3N_5. Two small peaks were observed at 1085 and 1161 cm^{-1} due to the mixed vibration of heptazine motif and azo stretch (Figure S5d). A sharp peak at 1609 cm^{-1} originated due to the C=N stretching mode.

Figure 7a displays the diffuse reflectance UV-Vis (DR-UV-Vis) spectra of g-C_3N_4 and C_3N_5. The DR-UV-Vis spectra of g-C_3N_4 shows a characteristic absorption peak between 200–400 nm with a band tail extended up to 450 nm due to charge transfer from the populated valence band of the nitrogen atom (2p orbitals) to the conduction band of the carbon atom (2p orbitals) of carbon nitride. The less intense absorption band at 330 nm is due to $\pi \rightarrow \pi^*$ transition in the conjugated network while another intense peak at *ca.* 387 nm appeared due to $n \rightarrow \pi^*$ transition from nitrogen nonbonding orbital to the aromatic nonbonding orbital.[12b, 42-44] The DR-UV-Vis spectrum of C_3N_5 demonstrates a drastic change in the UV-Vis absorption profile in comparison to g-C_3N_4 due to a more extended π conjugated network (Figure 7a).[12b, 45] A broad absorption peak around 393 nm in UV-Vis spectrum of C_3N_5 was attributed to $n \rightarrow \pi^*$ transition from nitrogen nonbonding orbital to the π conjugated nonbonding orbital. The absorption spectrum of C_3N_5 was red shifted showing band tailing up to 670 nm, due to an extended π conjugated network arising from the overlap between N2p orbitals of bridging azo moieties and N2p in heptazine π conjugated system. Further residual $-NH_2$ also contributes to the delocalized aromatic π conjugated system. Due to this, the position of the valence band gets upshifted and $\pi \rightarrow \pi^*$ transition occurs at relatively low energy which facilitates the absorption of a large fraction of the visible spectrum and results in the sample displaying an orange color. Further, the optical bandgaps of g-C_3N_4 and C_3N_5 were determined using a Tauc plot by plotting a graph between $(\alpha h\nu)^{1/2}$ *vs* $h\nu$ and extrapolation of the linear tangent to abscissa; where α is absorption coefficient, h is plank constant and v is light frequency (Figure S6a). From the Tauc plot, the value of bandgap for g-C_3N_4 was estimated to be 2.65 eV corresponding to a band-edge at a wavelength of 467 nm, in good agreement with the bandgap values reported in the literature.[46] The bandgap value of C_3N_5 was calculated to be 1.76 eV corresponding to a band-edge at a wavelength of 707 nm.

Photoluminescence (PL) spectra were collected by exciting samples using 360 nm photons to probe radiative recombination (Figure 7b). The PL spectrum of melem consists of an intense emission peak centered at 441 nm which is indicative of radiative recombination of carriers within melem unit.[39a, 44] It is important to note here that melem exhibits excitation wavelength-dependent PL emission. On the other hand, g-C_3N_4 showed a sharp emission peak at 468 nm which did not shift upon changing the excitation wavelength. This peak is attributed to fast interlayer carrier recombination in multilayered sheets of bulk g-C_3N_4.[45, 47] Surprisingly, C_3N_5 does not exhibit any distinguishing PL peak which might be indicative of efficient charge separation between the bulk and the surface. Such charge transfer excitonic states involving the bulk and the surface, have also been observed in other conjugated organic semiconductors that possess an extended π-conjugated network that prevents radiative recombination by delocalizing the Frenkel exciton. However, due to conductive conjugated surface non-radiative charge recombination can take place over new localized states in the sheets scaffold.[48]

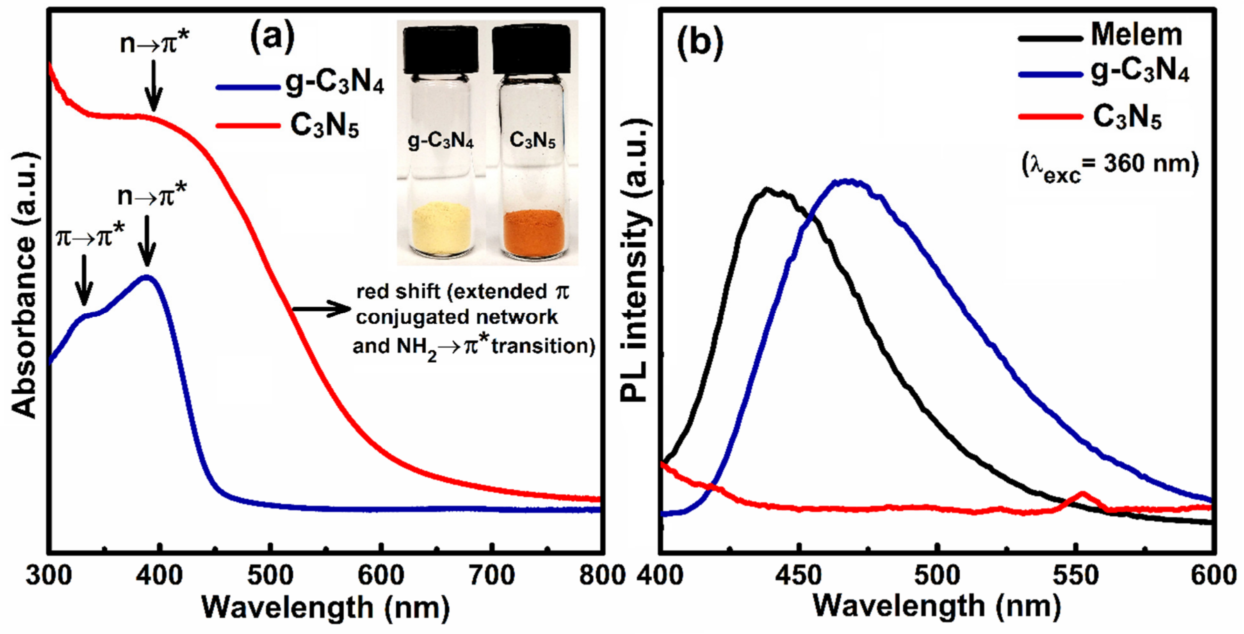

Figure 7. (a) DR-UV-Vis spectra of g-C_3N_4 (blue) and C_3N_5 (red), with inset showing photographs of g-C_3N_4 and C_3N_5 samples and (b) Steady-state PL spectra of melem (black), g-C_3N_4 (blue) and C_3N_5 (red) obtained using an excitation wavelength of 360 nm.

In order to investigate the lifetime of excited charged species, and charge separation processes, we collected time resolved photoluminesece (TRPL) spectra of g-C_3N_4 and C_3N_5 using a single photon picosecond pulsed laser at a wavelength of 405 nm. Figure 8 displays the PL lifetime decay curves of g-C_3N_4 and C_3N_5. The PL decay curve was fitted tri-exponentially using the following equation:

$$I(t) = A_1 e^{-t/\tau 1} + A_2 e^{-t/\tau 2} + A_3 e^{-t/\tau 3} \qquad (1)$$

where, A_1, A_2, and A_3 represent the normalized amplitudes of each decay component and τ_1, τ_2 and τ_3 are values of the lifetime components respectively. The existence of three radiative lifetimes in the fitted PL lifetime spectra of g-C_3N_4 and C_3N_5 was in good agreement with previously reported carbon nitride-based materials. [49] The obtained values of lifetimes and their fractional components are given in Table 2.

Table 2. The PL lifetime of phogenerated charge carrier and their relative contribution in g-C_3N_4 and C_3N_5.

Sample	**τ_1(ns) [A_1]**	**τ_1(ns) [A_1]**	**τ_1(ns) [A_1]**	**Average lifetime (τ_{avg}) ns**
g-C_3N_4	3.31 [0.34]	0.75 [0.63]	25.02 [0.05]	12.43
C_3N_5	8.10 [0.07]	2.11 [0.26]	0.28 [0.73]	4.40

The three components in the PL lifetime decay curve of g-C_3N_4 can be assigned to various energy states in g-C_3N_4 formed by the overlap of C and N sp^2 and sp^3 hybridized orbitals and the presence of lone pairs of electrons which allow for various radiative transitions. g-C_3N_4 is composed of tri-s-triazine (C_6N_7) units inter-connected with tertiary nitrogen atoms where C-N sp^3 hybridized state constitute high energy σ and σ* molecular orbitals while C-N sp^2 hybridization gives rise to a conjugated network resulting in low energy π bonding and π* antibonding orbital which constitutes the valence and conduction bands respectively.[50] The presence of unbonded lone pairs of electrons on pyridinic N atoms creates energy levels just below the π bonding orbital and their overlap with the π conjugated system can further decrease the energy of the π molecular orbital resulting in the reduction of the bandgap.[51] The first two shorter lifetime components of 3.31 and 0.75 ns with 34 % and 63 % contribution in g-C_3N_4 correspond to charge carrier recombination from σ* and π* antibonding to π MO.[52] The third longer lifetime component of 25.02 ns with a relative low contribution originated due to intersystem crossing (ISC) of electron from σ* and π* orbital followed by radiative relaxation to conjugated π orbital and trap-assisted radiative recombination.[53] The first two lifetimes of C_3N_5 at 8.10 and 2.11 ns with 7 % and 26 % contributions in the PL decay curve were significantly longer lived in comparison to g-C_3N_4, strongly suggesting that the introduction of azo moiety extends π conjugated network which facilitates better charge carrier mobility on C_3N_5 sheets (delocalized the exciton, as mentioned previously) and prevents faster charge carrier recombination.[54] Further, due to extended conjugation, the difference between σ* and π* band get decreased which is also evident in Mott-Schottky measurement (Figure S6b).[51a] The low energy difference between σ* and π* accelerates the transfer of electrons from σ* and π* orbital via intersystem crossing followed by radiative relaxation which was evident from higher percentage contribution of the third lifetime component (73 %).

The average lifetime (τ_{avg}) which is regarded as coherent measure to evaluate the rate of spontaneous emission was calculated from the three lifetime components using the following expression.

$$\tau_{avg} = (A_1\tau_1^2 + A_2\tau_2^2 + A_3\tau_3^2)/ (A_1\tau_1 + A_2\tau_2 + A_3\tau_3) \qquad (2)$$

From Eq (2), the average lifetimes of g-C_3N_4 and C_3N_5 were calculated to be 12.43 and 4.40 ns respectively. The decreased lifetime of the C_3N_5 in comparison to g-C_3N_4 coupled with the very weak photoluminescence of C_3N_5 (as seen in Figure 7b) is indicative of fast quenching of the C_3N_5 luminescence. The fast quenching might originate from improved charge separation in C_3N_5 due to a larger conjugated π network but might also be due to stronger non-radiative transitions. Fast exciton dissociation with concomitant high carrier mobility can result in photogenerated electrons finding trap sites (and moving to them) and recombining by non-radiative processes.[48a] The aforementioned processes are highly likely in C_3N_5 since the presence of azo bonds extends the π network because of overlap of N2p orbital on azo nitrogens with the π network of heptazine motif due to which electrons can move within C_3N_5 scaffold freely. The lower PL lifetime of C_3N_5 in comparison to g-C_3N_4 was consistent with steady-state PL where C_3N_5 shows prodigious quenching in its PL spectrum.

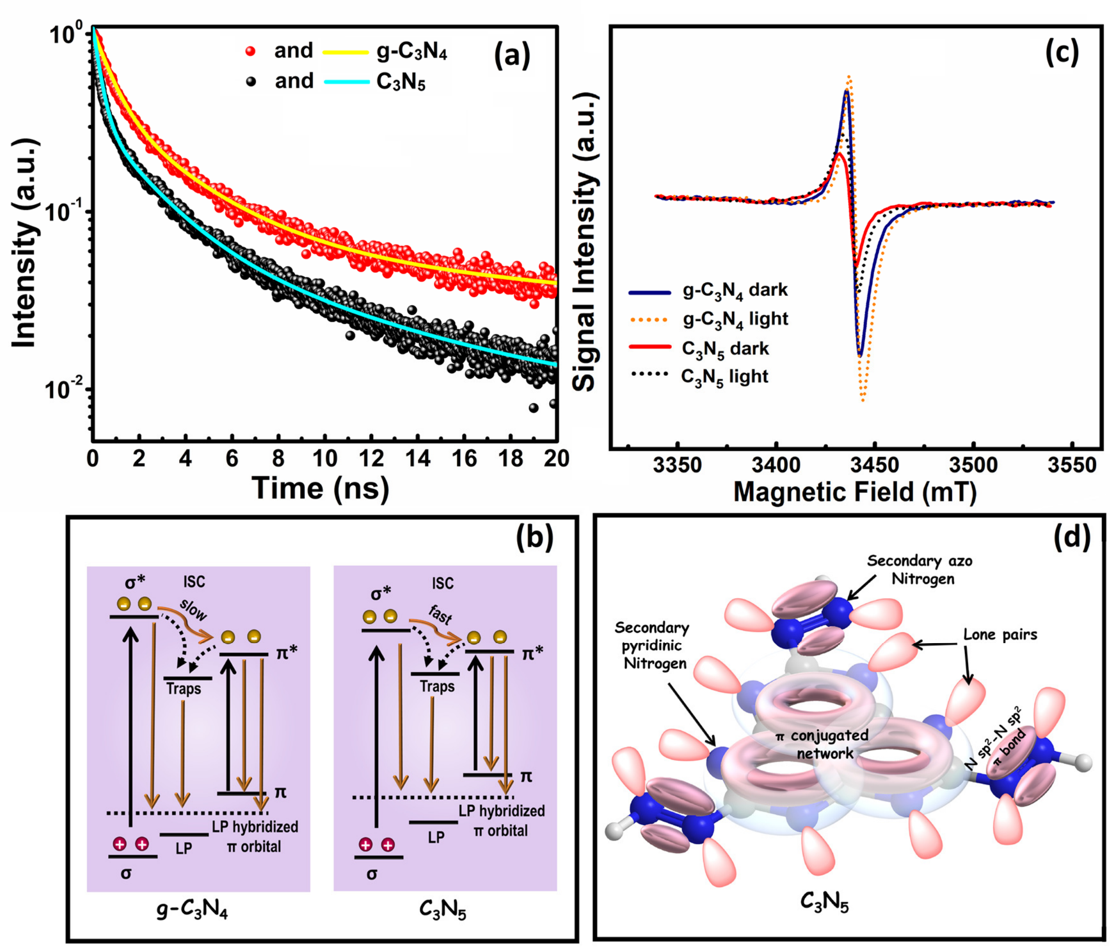

Figure 8. (a) PL lifetime decay curves of g-C_3N_4 (red; tri-exponential fit, yellow line) and C_3N_5 (black, tri-exponential fit, cyan), (b) Schematics of various energy levels bands and possible route of charge carriers recombination (c) X-band EPR spectra of g-C_3N_4 in the dark (blue), after light irradiation (orange dots) and C_3N_5 in the dark (red) and after light irradiation (black dots) at room temperature, (d) Plausible molecular orbital overlap representation of C_3N_5.

Electron paramagnetic resonance (EPR) spectra of g-C_3N_4 and C_3N_5 to elucidate electronic nature and band excited paramagnetic species were collected under dark and UV irradiation at room temperature (Figure 8b). The EPR spectra of g-C_3N_4 under dark conditions exhibits an intense Lorentzian EPR resonance signal located at a g-factor of 2.003. The observed EPR signal originated due to the presence of unpaired electrons in the sp_2 hybridized aromatic π-system which was in good agreement with previous reports.[36, 55] The EPR signal intensity of g-C_3N_4 increased after UV irradiation, attributed to populated unpaired electrons in the conduction band due to π-π* and N non-bonding to π* (n-π*) transition followed by slow relaxation *via* ISC. The observed EPR signal of C_3N_5 was also observed at 2.003 g-value which implies basic graphitic heptazine skeleton remains intact in C_3N_5 framework.[56] Further, after irradiation with UV light, the EPR signal intensity of C_3N_5 was also enhanced due to increased numbers of unpaired electrons in the conduction band. However, the overall EPR signal intensity of C_3N_5 in both the dark and under UV illumination was significantly weaker in comparison to g-C_3N_4 which was attributed to a lesser number of unpaired electrons in C_3N_5, which in turn can be taken as evidence of the presence of extra N atoms outside the heptazine nucleus in comparison to conventional N-rich carbon nitride materials where N atoms substitute C atoms in the heptazine motif. It is well documented in the literature that substitution of sp^2 hybridized +4 state C atom in heptazine motif with sp^2 hybridized +3 state N atom will liberate extra electrons in the aromatic system which will distort electronic symmetry [16, 47, 57] and also increase EPR signal intensity. However, in the case of C_3N_5, the additional N atom makes an azo bond with an N atom outside the ring via π overlap and the extra electrons remain in the form of lone pairs (Figure 8d).

Fluorescence lifetime imaging microscopy (FLIM) of samples at different spots was used to probe the homogeneity of samples and to determine the nature of the fluorescence (Figure S7).

The PL spectra of g-C_3N_4 samples obtained from different spots exhibited identical emission profiles with a sharp intense peak at 480 nm which was in good agreement with the steady-state PL spectrum (Figure 7b). The slight red shift in the emission peak (Figure S7a) is attributed to the difference in the mechanism of excitation (750 nm two-photon excitation source for FLIM, 360 nm single photon excitation in Figure 7b). Furthermore, the emission spectrum of C_3N_5 displays two relatively weak peaks centered around 410 and 490 nm which likely originated from some relatively smaller C_3N_5 polymeric fragments and heptazine networks (Figure S7c). The smaller fragments are consistent with a lesser number of MH units and therefore exhibit PL properties closer to melem. FLIM images of g-C_3N_4 were brighter than C_3N_5 which further supports our inference that the charge separation process was dominant in C_3N_5 samples (Figure S7b and Fig. S7d). The C_3N_5/MB samples obtained after methylene blue (MB) dye adsorption displayed relatively strong PL and brighter FLIM images due to the presence of MB in the composite (Figure S7e and Figure S7f). The absence of PL quenching in the C_3N_5/MB composite further suggests the absence of photo-induced charge transfer between the methylene blue and C_3N_5.

The synthesized C_3N_5 material was explored for dye adsorption studies using methylene blue (MB) as a model dye. Methylene blue is a staining dye widely used in the paper, textile and leather industries which also constitutes a good example of a colored water contaminant which due to its excellent visible light absorption, reduces light penetration in aqueous ambients and adversely affects aquatic flora and fauna. All dye adsorption studies were carried out at room temperature and under dark conditions. UV-Vis spectra of samples were collected for determining the concentration of MB solutions during dye adsorption experiments (For experimental details, see supporting information). MB has a sharp peak at 664 nm due to π-π^* transition and a shoulder around 614 nm which represents MB present in dimeric and polymeric π stacked forms in water

(Figure 9a). After the addition of C_3N_5 sample into methylene blue solution, the color of the solution instantaneously turned green. The green solution after centrifugation turned completely colorless which demonstrated the prompt adsorption of MB dye over the surface of C_3N_5 and subsequent settling of the MB adsorbed C_3N_5 during centrifugation. The obtained solid after centrifugation (denoted as C_3N_5/MB) exhibits a sharp absorption peak intermediate between C_3N_5 and MB with a broad peak centered at 680 nm. The redshifting in the peak of C_3N_5 from 664 to 680 nm is attributed to the transformation of MB into monomeric form and some degree of ground state charge transfer from C_3N_5 to MB during adsorption on the surface of C_3N_5. The dye adsorption performance of C_3N_5 was much higher than g-C_3N_4. MB is a well known cationic dye possessing positive charge centered on the S atom in aqueous solutions.[58] On the other hand, the surface of C_3N_5 material has electron rich character due to the presence of secondary N (NC_2) in heptazine moieties, terminal $-NH_2$ and π extended network. Therefore, electrostatic interactions between the positively charged MB molecule and negatively charged C_3N_5 are likely responsible for the instantaneous adsorption.[54, 59] To confirm negative charge on the surface of C_3N_5, zeta potential measurement was performed which depicts average surface charge –36.2 mV prove the electron-rich surface of C_3N_5 (Figure S8). Further MB can also adsorb on the surface of C_3N_5 via π-π stacking between aromatic conjugated network of MB and π framework of C_3N_5 (Figure 9b).[60] To investigate the role of surface specific properties in the enhanced adsorption profile, Brunauer-Emmett-Teller (BET) surface area (S_{BET}), pore volume (V_p) and pore diameter (r_p) of g-C_3N_4 and C_3N_5 were measured by N_2 adsorption and desorption. The obtained BET surface area, pore volume and pore diameter for g-C_3N_4 were found to be 11.47 m^2 g^{-1}, 0.095 cm^3, and 19.13 nm while these values for C_3N_5 were found to be 1.78 m^2 g^{-1}, 0.002 cm^3 g^{-1} and 16.98 nm, respectively. The obtained surface values indicate a decrement in the surface area of C_3N_5 in comparison to g-

C_3N_4. The relatively low surface area of C_3N_5 might be due to the less gas evolution (three NH_3 per heptazine unit) from melem hydrazine precursor during thermal annealing step while the formation of g-C_3N_4 from melamine precursor releases six NH_3 molecule per heptazine unit. Further, hydrogen bonded melem hydrazine precursor might promote in-plane cross-linking of heptazine units leading to a stacked sheets type structure which reduces the effective accessible surface area. Contrarily, in g-C_3N_4 ring formation and polymerization step can produce cross-linking between sheets giving a porous structure with high surface area. The obtained results suggest that an electronic interaction between C_3N_5 and MB is responsible for the superior adsorption performance of C_3N_5 rather than an increased surface area.

To investigate whether the nature of adsorption was chemisorption or physisorption, and to explore the possibility of any chemical bonding, the C_3N_5/MB composite was analyzed using NMR spectroscopy. The ^{13}C NMR spectrum of C_3N_5/MB composite did not show any change in peak position and intensity of C_3N_5 which demonstrated the adsorption of MB on C_3N_5 to be purely physisorptive in nature (Figure S9d). FTIR, Raman and PL spectra of C_3N_5/MB composite displayed various cumulative peaks and signals due to the presence of MB in the C_3N_5/MB composite. However, no evident signals for any chemical interaction can be identified which further supports a purely physical interaction (physisorption) between C_3N_5 and MB (Figure S9a-c). Additionally, XPS spectra of C_3N_5/MB composite were identical to pristine C_3N_5 samples which revealed that C_3N_5 signals dominated over MB, and no change in BE value was observed which ruled out the possibility of any chemical bond formation between C_3N_5 and MB (Figure S10).

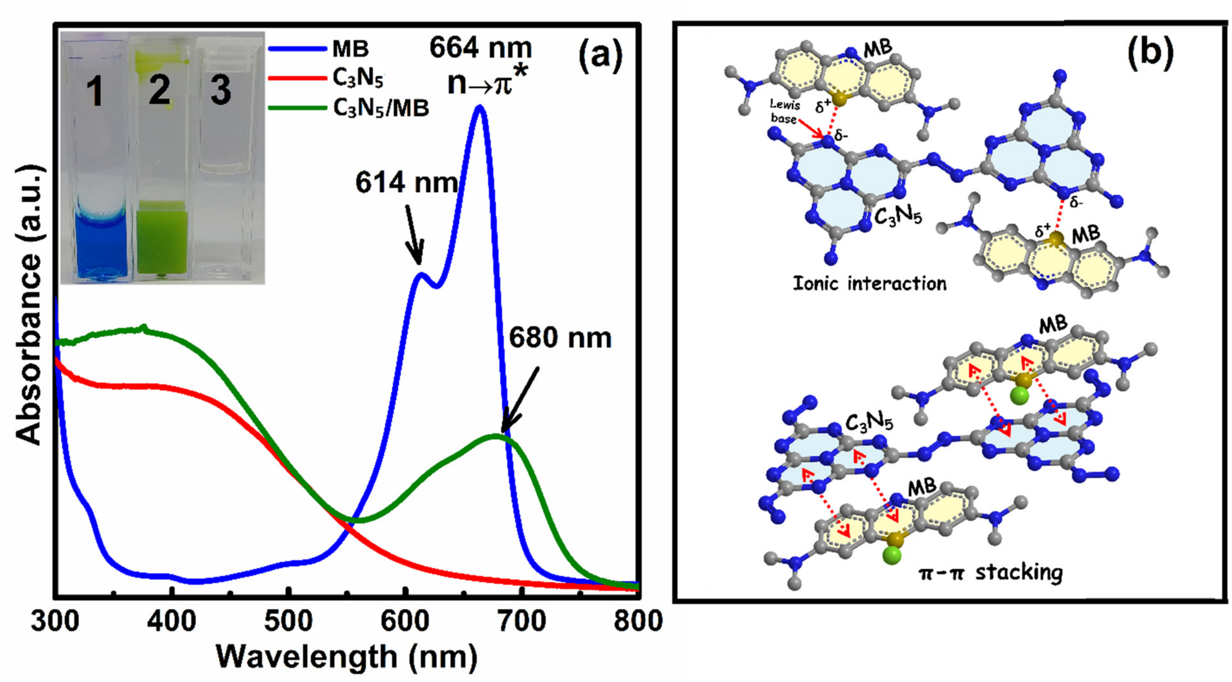

Figure 9. (a) UV-Vis absorption spectra of MB (blue), C_3N_5 (red) and C_3N_5/MB solution just after 1 min of absorption (green). Inset showing photographs of (1) MB before absorption, (2) after absorption and (3) solution after centrifugation, (b) Possible ionic and π-π stacking interaction between methylene blue and C_3N_5.

To quantify the excellent dye adsorption capacity of C_3N_5, various parameters such as the adsorption capacity, adsorption constants, linear regression correlation coefficient, and adsorption isotherm were measured and compared with pristine g-C_3N_4 (Figure 10 and Table 3). The adsorption capacity (amount of dye adsorbed) of g-C_3N_4 and MHP materials was calculated using equation 3

$$q = \frac{(C-C_e)V}{m} \tag{3}$$

Where q is the adsorption capacity, V is the volume of MB solution, m is the mass of the added adsorbent, and C and C_e are the initial and equilibrium concentrations of MB, respectively. The kinetics of methylene blue adsorption on the surface of g-C_3N_4 and C_3N_5 were investigated using first and second order adsorption kinetics using following equations 4 and 5.

$$q_t = q_e(1 - e^{-kt}) \qquad (4)$$

$$q_t = \frac{kq_e^2t}{1+kq_et} \qquad (5)$$

Where q_e is adsorbed amount of dye after reaching equilibrium and q_t is the adsorbed amount at time t, and k is the pseudo-first order or pseudo-second order adsorption rate constant.

The results obtained using pseudo-first order and pseudo-second order kinetics are displayed in Table 3 and Figures 10a and 10b. The kinetic studies clearly demonstrate that the prepared C_3N_5 samples can reach approx. 95% adsorption-desorption equilibrium instantaneously (1 min), and complete adsorption-desorption equilibrium condition within 10 min, which is an extraordinary performance compared to previously reported carbon nitride and carbon-based materials which usually take 45 min to achieve equilibrium.[61] In addition, the kinetics study indicated that the adsorption of methylene blue on the C_3N_5 and g-C_3N_4 materials follows pseudo-second order adsorption kinetics, which agreed well with previous reports.[61a] For isotherm studies, standard solutions of 5, 10, 15, 20, 25 and 30 ppm MB in water were prepared, 50 mL of these standard solutions were placed in a beaker and 50 mg of the adsorbents were added to them. The solutions were kept under strong stirring for 30 min under dark condition to reach equilibrium and then the concentration of methylene blue was calculated using UV-Vis spectroscopy (See Supporting Information for detail). The adsorption isotherms of methylene blue were investigated in terms of the Langmuir[61b, 62] and Freundlich models[61b, 63] (equations 6 and 7 respectively) and the results for g-C_3N_4 and C_3N_5 are displayed in Figures 10c and 10d respectively; the relevant constants are reported in Table 3. It can be seen from Figure 10 and Table 3 that the value of R^2 extracted by employing the Langmuir isotherm model was higher than R^2 value obtained from the Freundlich isotherm model, indicating that the Langmuir model representing complete monolayer coverage on homogeneous sites was successful in predicting the adsorption of methylene blue on both g-C_3N_4 and C_3N_5.[64]

$$q_e = \frac{QbC_e}{(1+bC_e)} \tag{6}$$

$$q_e = KC_e^n \tag{7}$$

Where q_e is adsorbed amount of dye after reaching equilibrium (mg g^{-1}), R is correlation coefficient, Q is the monolayer adsorption capacity (mg g^{-1}), b is the adsorption coefficient (L mg^{-1}), C_e is the equilibrium concentration and K is the Freundlich constant.

Table 3. The pseudo-first and -second order kinetic models of MB adsorption on g-C_3N_4 and C_3N_5 and Langmuir and Freundlich adsorption models showing isotherm constants.

Serial No.	**Sample name**	**Pseudo-first-order**			**Pseudo-second-order**		
		k (s^{-1})	***q_e*** (mg g^{-1})	***R^2***	***k*** (s^{-1} mg^{-1} L)	***q_e*** (mg g^{-1})	***R^2***
1.	g-C_3N_4	0.16	2.35	0.96	0.08	2.6	0.99
2.	C_3N_5	6.35	6.83	0.98	2.24	6.95	0.99
S.No.	**Sample name**	**Langmuir**			**Freundlich**		
		Q (mg g^{-1})	***b*** (L mg^{-1})	***R^2***	***K*** (mg^{1-n} L^n g^{-1})	***n***	***R^2***
1.	g-C_3N_4	6.03	0.13	0.97	1.21	0.43	0.96
2.	C_3N_5	42.32	0.05	0.98	2.40	0.78	0.97

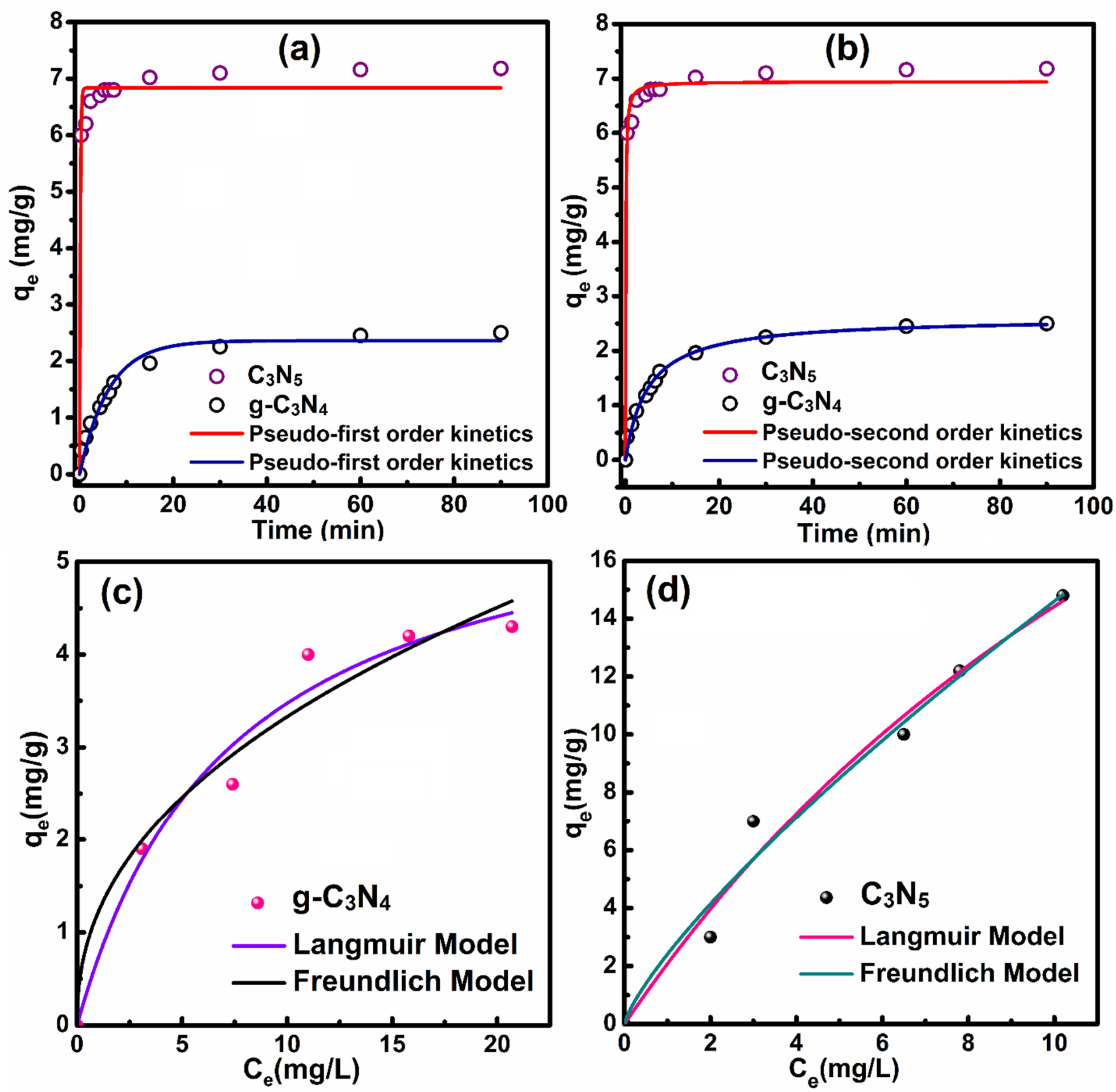

Figure 10. Kinetics of MB dye adsorption on g-C_3N_4 and MB displaying (a) Pseudo-first order fitted curve (b) Pseudo-second order fitted curve and MB adsorption isotherms fitted by Langmuir and Freundlich model of (c) g-C_3N_4 and (d) C_3N_5 respectively. q_e is the amount of dyes adsorbed at equilibrium while C_e is the equilibrium concentration of MB.

To check whether C_3N_5 material displays any visible light induced dye degradation activity, 50 mL of 50 ppm MB containing solution was charged with 50 mg C_3N_5 catalyst and stirred in the dark for 30 min to reach adsorption-desorption equilibrium. Subsequently, the obtained suspension was irradiated under simulated sunlight (AM1.5G, 100 mW cm^{-2}). After every 10 min, 1 mL of sample was withdrawn and centrifuged to remove solid C_3N_5 and the supernatant liquid was analyzed with UV-Vis spectroscopy. The UV-Vis analysis indicated that the concentration of MB solution does not change even after 8 h of irradiation. These results suggest that C_3N_5 is not active for dye degradation which might be because of unfavorable band alignment. To understand the band structure of C_3N_5, Mott Schottky plots were obtained in 0.5 M Na_2SO_4 solution (Figure S6b). From the Mott-Schottky plot, the flat band positions of g-C_3N_4 and C_3N_5 were found to be –1.05 and –0.91 V *vs* Ag/AgCl, respectively, which can be considered the conduction band position if the Fermi level lies just below conduction band (strong *n*-type character). Using the bandgap values obtained from the Tauc plot (2.65 eV for g-C_3N_4 and 1.76 eV for C_3N_5), the positions of the valence band edge for g-C_3N_4 and C_3N_5 were calculated to be +1.60 and +0.85 V *vs* Ag/AgCl, respectively. Since the standard band edge positions are usually expressed with reference to NHE, the CB and VB positions of g-C_3N_4 were calculated to –0.85 and +1.80 V *vs* NHE at pH-0, while CB and VB positions of C_3N_5 were found to be –0.72 and +1.04 V *vs* NHE at pH-0.

XPS valence band spectra of C_3N_5 was collected to get further information regarding the band structure (Figure 11a). The intersecting point obtained by extrapolation of XPS VB spectra on X and Y axis gave the value of valence band maximum (VB_{max}). The VB_{max} of C_3N_5 was calculated to be +0.95 eV which was approximately the same (+1.05 V) obtained from the Mott-Schottky measurements and UV-Vis data. Further, by using XPS VB and optical bandgap (1.76

eV) values, the CB_{min} and VB_{max} of C_3N_5 were calculated to be –0.79 and +0.97 eV, while for g-C_3N_4, CB_{min} and VB_{max} positions were found to be -0.85 eV and +1.80 eV respectively. Figure 11b a schematic illustration of the density of states (DOS) distribution in C_3N_5 and g-C_3N_4.

The dye degradation process begins with the reaction with •OH radical originating from photogenerated holes in the valence band of the semiconductor. The oxidation potential of water to generate •OH radical (H_2O/•OH) is +2.38 V *vs* NHE at pH-0 which requires highly oxidative holes. Another route for the generation of •OH radicals is the reduction of O_2 to $O_2^{\bullet-}$ anion radical ($O_2/O_2^{\bullet-}$, –0.33 V *vs* NHE at pH-0) at the conduction band followed by reaction with protons to afford •OH radicals.[63, 65] However for this process required protons should be derived from water oxidation (H_2O/O_2, +1.23 V *vs* NHE at pH-0).[64, 66] Unfortunately, the valence band position of C_3N_5 is just +1.04 V *vs* NHE which cannot facilitate water oxidation thus explaining the absence of photocatalytic activity for MB degradation. Nyquist plots of g-C_3N_4 and C_3N_5 determined with electrochemical impedance spectroscopy (EIS) under dark and AM1.5G irradiation demonstrate that the semicircle for C_3N_5 was larger than for g-C_3N_4 which represents a higher charge transfer resistance in C_3N_5 compared to g-C_3N_4; a higher charge carrier recombination is indicated in C_3N_5 (Figure S11).

Due to the unfavorable band edge positions of C_3N_5 (CB = –0.71 V and VB = +1.04 V *vs* NHE at pH-0), it is not able to function as a stand-alone catalyst for the photoelectrochemical splitting of water. However, the excellent visible light absorption of C_3N_5 encouraged us to investigate the photosensitizing effect of C_3N_5 to increase the photocatalytic performance of TiO_2 (a wide bandgap semiconductor).[67] The conduction band of C_3N_5 (–0.72 V *vs* NHE) was more negative than conduction band of TiO_2 (–0.1 V *vs* NHE) which favors transfer of photogenerated electrons in the CB of C_3N_5 to the CB of TiO_2.[68] To measure photosensitizing performance, C_3N_5, and g-C_3N_4 powders were mixed with TiO_2 nanoparticles in α-terpineol solution (film-forming agent) followed by drop-casting on FTO:glass substrates coated with a thin (~ 50 nm) blocking layer of TiO_2. A three electrode setup consisting of the samples as the photoanode (working electrode), Pt as cathode (counter electrode) and Ag/AgCl reference electrode was used for photoelectrochemical water splitting experiments in 0.1 M Na_2SO_4 electrolyte, while a Class A solar simulator was used as the source of AM1.5G simulated sunlight (100 mW cm^{-2}). Linear sweep voltammograms of electrodes consisting of C_3N_5 and pristine g-C_3N_4 samples mixed with TiO_2 NPs are shown in Figure 11a. It can be seen from Figure 11a that the photocurrent density for C_3N_5 sensitized TiO_2 was much higher than g-C_3N_4 sensitized TiO_2. The current density for C_3N_5 and g-C_3N_4 sample blended TiO_2 sample was found to be 152 and 100 µA cm^{-2} at an applied potential of +0.6 V *vs* NHE (or 1.23 V *vs* NHE). To probe the improved photosensitizing performance in the visible region, on-off experiments using a 450 nm LED (54.15 mW cm^{-2}) were carried out which clearly show the alternate drop and rise in photocurrents in on-off cycles (Figure 11b). Figure 11b also shows that the magnitude of the photocurrent was higher for the C_3N_5 sample. A similar pattern in the on-off cycle was observed when samples were irradiated with 505 nm LED (40.48 mW cm^{-2}) confirming the improved photosensitizing properties of C_3N_5 at longer wavelengths (Figure S12). Further, photoelectrochemical water splitting experiment carried out using Na_2S (2.0 mmol) as hole scavenger showed enhanced photocurrent density, reaching up to 465 µA cm^{-2} for C_3N_5 under AM 1.5 G irradiation (>420 nm) (Figure S13). Under identical conditions, the value of photocurrent density for g-C_3N_4 was found to be 373 µA cm^{-2} (Figure S13a). Similar pattern was followed at higher wavelengths and calculated current density for C_3N_5 was found to be 454 and 145 µA cm^{-2} at 450 and 505 nm, while for g-C_3N_4 the value of current density was found to be 275 and 80 µA cm^{-2} respectively (Figure S13b) Photocurrent response of

C_3N_5 as function of time during light on-off cycle doesn't change significantly compared to g-C_3N_4 which demonstrate resiliency of C_3N_5 under reaction conditions and charge flow (Figure S14). The maximum applied bias photon-to-current efficiency (ABPE) and incident photon-to-current efficiency (IPCE) achieved by C_3N_5 was 0.059 and 2.33% (at 450 nm) while these value for g-C_3N_4 was 0.048 and 1.41% (at 450 nm), respectively (Figure S13c and d).

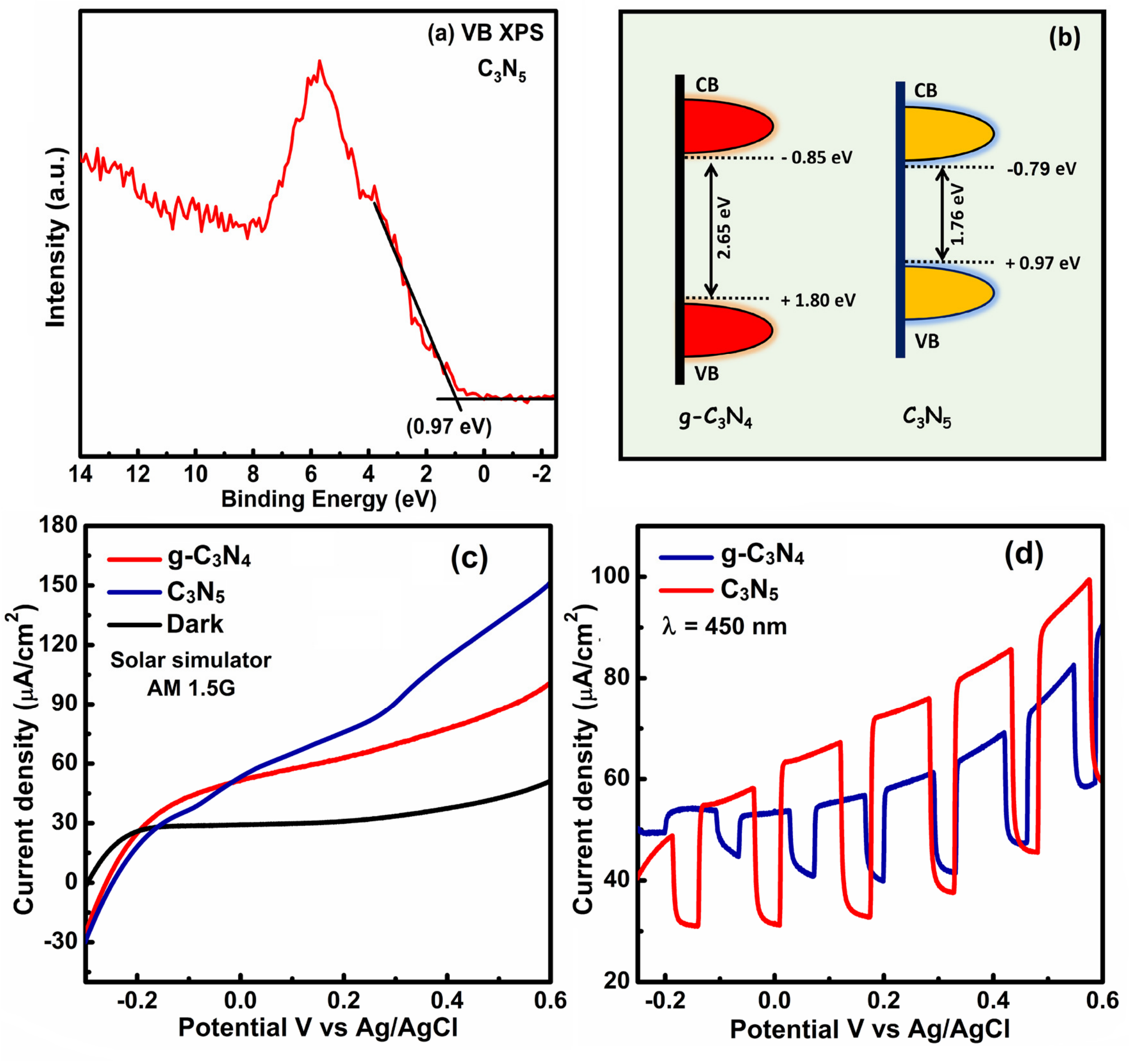

Figure 11. (a) XPS valence band spectra of C_3N_5 for determining energy levels (b) Density of state revealing band structure of g-C_3N_4 and C_3N_5 (c) Linear sweep voltammogram showing current-potential characteristics of g-C_3N_4 (blue) and C_3N_5 (red) measured in 0.1 M Na_2SO_4 solution AM1.5G light irradiation (100 mW cm^{-2}) and

under dark condition (d) Light on-off showing photocurrent response *vs* applied voltage by using 450 nm wavelength light (54.15 mW cm^{-2}) for g-C_3N_4 (blue) and C_3N_5 (red).

To demonstrate the optoelectronic application of our newly synthesized graphenic semiconductor, we employed C_3N_5 as the electron transport layer (ETL) in $MAPbBr_3$ based perovskite solar cells and obtained a good result. Carbon-based materials have frequently been used as hole transport layers (HTLs) or hole collection electrodes in $MAPbBr_3$ based solar cells, but have almost never been used (effectively) as ETLs to boost the open circuit photovoltage. Using C_3N_5 as the ETL and with no optimization of any kind, we measured a V_{oc} of 1.3 V, J_{sc} of 7.5 mA cm^{-2} and a FF (fill factor) of 0.4 to obtain a power conversion efficiency (PCE) of 4.2 % (Figure S15 and S16 in Supporting Information). Some context is needed to appreciate the significance of the aforementioned result. Methylammonium lead bromide ($MAPbBr_3$) is a halide perovskite with an electronic bandgap of 2.23 eV which has two major advantages for solar cell applications in comparison to the more commonly used methylammonium lead iodide ($MAPbI_3$) – in theory, it enables the construction of much higher V_{oc} solar cells that can be used to power electrocatalytic and electrochemical reactions and secondly, $MAPbBr_3$ is known to have superior ambient stability (less moisture sensitivity) and operational stability (due to the absence of phase transitions and enhanced thermal stability at a high working temperature) compared to $MAPbI_3$.[69] However, until recently, most works in this area failed to achieve the expected high V_{oc} value, and the typical V_{oc} values obtained using were in the range 0.90-1.16 V.[70] The use of carbon-based charge transport layers has enabled a dramatic improvement in the performance of $MAPbBr_3$-based photovoltaic devices by generating photovoltages in excess of 1.3 V (as high as 1.6 V) without suffering a corresponding penalty in the short circuit current (J_{sc}). The first such report was by Wu *et al.*[71] wherein indene-C60 bisadduct (ICBA) was used as the acceptor in conjunction with $MAPbBr_3$ to realize a high V_{oc} perovskite solar cell. Shortly thereafter, Li *et al*. used carbon nanotubes as an efficient hole collector for $MAPbBr_3$ solar cells and achieved a V_{oc} of 1.4 V.[72] $MAPbBr_3$ sandwiched between modified PEDOT:PSS (hole transport layer) and $PC_{61}BM$ (electron transport layer) resulted in a solar cell with a V_{oc} of 1.52 V[73] while a graphitic carbon anode (with no hole transport layer) and TiO_2 electron transport layer were used by Liang *et al.* to realize a $MAPbBr_3$ solar cell with a V_{oc} as high as 1.57 V.[74]

The origin of the poor V_{oc} values was poorly understood for a long time. Even now, there are two distinct explanations, one based on active layer material quality issues and another based on high interfacial recombination. For instance, vapor deposited $MAPbBr_3$ films were found to generate high V_{oc} values in comparison with solution-deposited films, which was attributed to the superior morphology and grain size in the vapor deposited films, and supported the explanation based invoking material quality.[75] The second explanation was supported by the observation of high V_{oc} values when hole transport layers with deep HOMO levels were used, indicating that the separation of the electron- and hole- quasi-Fermi levels at the charge extraction interfaces, was the controlling mechanism determining V_{oc}.[76] Our examination of $MAPbBr_3$ solar cells using C_3N_5 as the ETL provides a way to reconcile the above explanations. On the one hand, the high CB position of C_3N_5 is better aligned with the CB of $MAPbBr_3$, and enables an optimal value for the electron quasi-Fermi level at the perovskite- C_3N_5 interface. On the other hand, the low dark current observed using C_3N_5 ETL in comparison to both TiO_2 and g-C_3N_4 ETLs (Figure S17 in Supporting Information) indicates suppression of trap-mediated hopping through $MAPbBr_3$ due to the insertion of C_3N_5 as a midgap state-free barrier layer, thus enabling the circumventing of active layer material quality issues. In summary, it is noteworthy that an unoptimized ETL made with a brand new semiconductor (C_3N_5) that was cast into films from a particulate suspension, generated a V_{oc} value of 1.3 V, higher than that generated by TiO_2 and g-C_3N_4 ETLs.

The photovoltaic performance of halide perovskite solar cells is highly dependent on grain size and defects free lattice states and presence of small numbers of defects and trap sites have a detrimental effect. The trap assisted recombinations can be minimized by passivating perovskite layer with graphenic materials due to their high carrier mobility and surface area materials which can efficiently capture charge are improve transportation behavior resulting in better photoconversion efficiency.[77] Further, incorporation of graphenic semiconductors with perovskite precursor provide crystallization surface which helps in increasing of grain size and minimize defects density at grain boundaries. The increased conjugation in C_3N_5 should lead to electron rich conductive surface with high charge carrier density and better carrier mobility than g-C_3N_4. To verify this assumption we have blended $MA_xFA_{1-x}Pb(I_{0.85}Br_{0.15})_3$ based perovskite with different wt% of C_3N_5 and g-C_3N_4. Under optimized conditions, 4 wt% doping of g-C_3N_4 and C_3N_5 with respect to PbX_2 was found best performing and C_3N_5 outperformed over g-C_3N_4 and bare PbX_2 based solar cell architecture attributed to better charge separation in more conjugated C_3N_5 scaffold and reduced trap sites.

Figure 12 shows the *J-V* curves of the best performing solar cells devices based on undoped and doped perovskite layers while the photovoltaic performance of solar cells is summarized in table 4. Solar cells made with a compact undoped perovskite solar cell yielded a short circuit current density (J_{sc}) of about 20.344 mA/cm^2, an open circuit voltage (V_{oc}) of 1.04 V and fill factor (FF) of about 66% resulting in the overall power conversion efficiency (PCE) of about 13.959%. While, perovskite solar cell made with g-C_3N_4-doped perovskite layer showed a J_{sc} of 21.573 mA/cm^2, V_{oc} of 1.03V and fill factor of about 69.1% and corresponding PCE of about 15.344%. C_3N_5 doped perovskite solar cells displayed PCE value of 16.689% resulting from V_{oc} of 1.065V, J_{sc} of 22.87 mA/cm^2 and FF of 68.5%.

Capacitance-voltage measurement on fabricated devices with doped/undoped perovskite layer was measured at 10 kHz frequency in dark to determine bulk properties such as doping density (N_D) and energy equilibrium at the contacts which is related to the flat-band potential (V_{fb}).[78] Mott-Schottky plots for the devices made with doped and undoped perovskite layer are shown in Figure 13.

$$\frac{1}{C_{sc}^2} = \frac{2}{e\varepsilon_0\varepsilon_r N_D}\left\{(V - V_{FB}) - \frac{kT}{e}\right\} \tag{8}$$

$$N_D = \frac{2}{e\varepsilon_0\varepsilon_r n} \tag{9}$$

V_{fb} and N_D were calculated by using equation (8) and equation (9) respectively, where C_{sc} is the space-charge capacitance (*i.e.* film capacitance) per unit area; ε_r is the dielectric constant of the material, ε_0 is the vacuum permittivity, *k* is Boltzmann constant, *T* is temperature in Kelvin, *e* is the electron charge and *V* is the applied potential. The measured V_{fb} of bare undoped, g-C_3N_4_doped and C_3N_5 doped perovskite solar cell was found to be 1.12, 1.08 and 1.15 V respectively, while carrier concentration of the respective devices was found to be 1.74×10^{16}, 1.96×10^{16} and 1.36×10^{16} cm^{-3}. This proves that doping perovskite layer with C_3N_5 significantly improves the charge transport in the device compared to the undoped and g-C_3N_4-doped devices.

To explore the charge transport characteristics, hole only devices with the architecture of FTO/PEDOT:PSS/Perovskite/Spiro-oMeTAD/Au was measured by the space charge limited current (SSLC) model described by the following equation.

$$J = \frac{9}{8L^3}\,\epsilon_0\epsilon_r\mu V^2 \qquad (10)$$

Where ϵ_0, ϵ_r, μ , and L are permittivity of the free space, relative permittivity of the perovskite, carrier mobility in the perovskite layer and thickness of perovskite layer respectively. The hole mobility in pure perovskite was found to be 2.55×10^{-3} cm^2/sS while that of g-C_3N_4 and C_3N_5 doped perovskite was found to be 3.28 $\times10^{-3}$ cm^2/Vs and 4.33×10^{-3} cm^2/Vs respectively (Figure S19).

To get insight into the charge transfer properties of perovskite solar cells based on undoped and doped perovskite layer, solid-state impedance spectroscopy measurements in the frequency range from 0.1 Hz to 1 MHz at different applied bias under dark condition were performed. The resulting Nyquist plots were fitted with the circuit shown in inset of Figure 12c, where R_s is series resistance, R_{rec} and C represents the resistance and capacitance at the interface between the active layer and charge transport layer and Q is a constant phase element (CPE) with coefficient N. The resulting recombination resistance of different solar cells obtained after fitting the Nyquist plot observed from the low-frequency region at different voltage shown in Figure 12 (d-i). C_3N_5 doped device showed a higher value of R_{rec} compared to the g-C_3N_4 doped and undoped devices. As the electron and hole transporting layers for all kind of devices are same, the difference in R_{rec} is mostly governed by the change in the interfacial property of perovskite layer induced by doping with C_3N_5 and g-C_3N_4. Interfacial recombination is inversely proportional to the recombination resistance, therefore, it can be concluded that the interfacial charge recombination in perovskite solar cells significantly gets suppressed by doping with MHP while it increases by doping with g-C_3N_4 resulting in an improved V_{oc} in C_3N_5 based device followed by the undoped and doped devices.

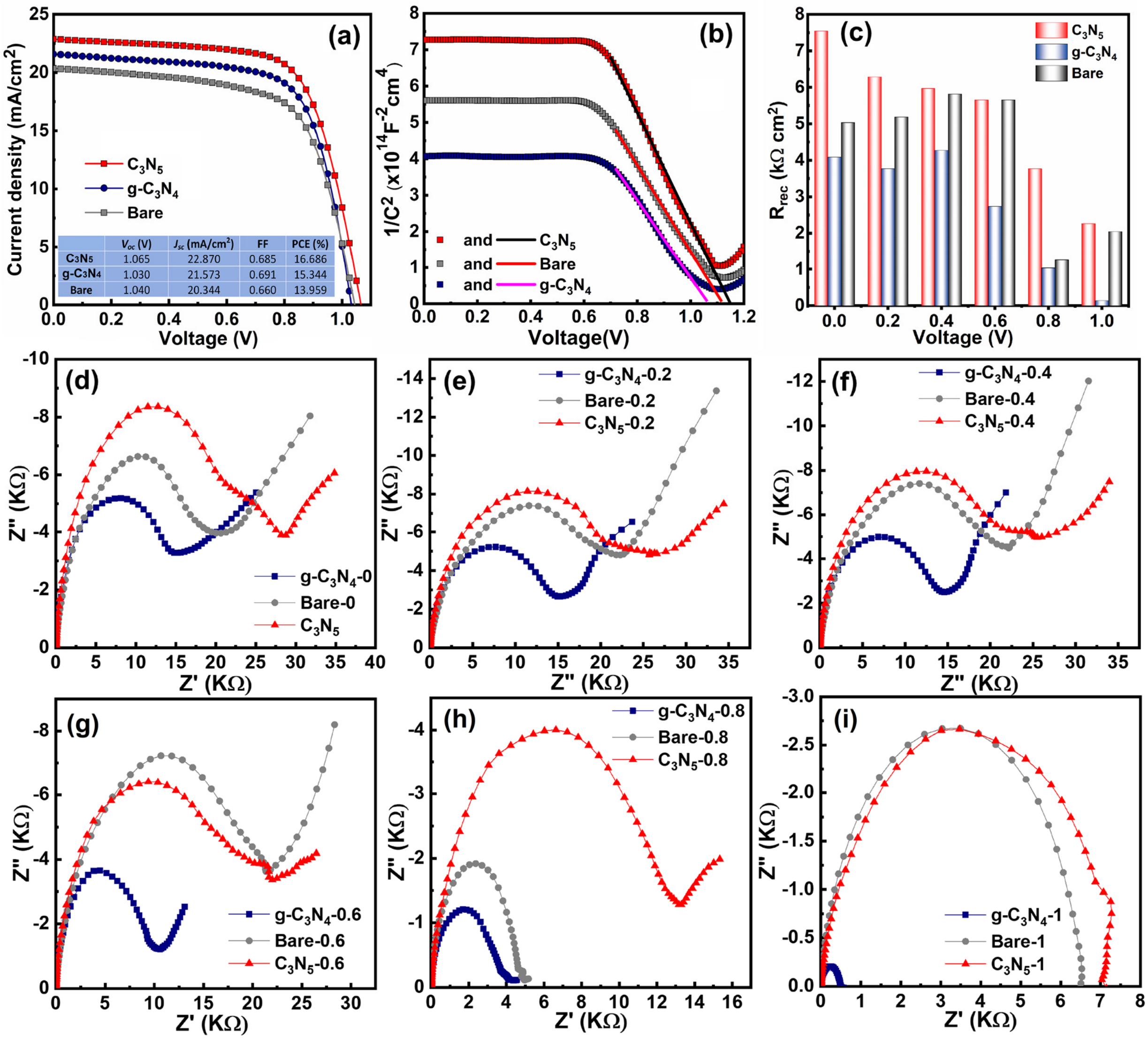

	V_{oc} (V)	J_{sc} (mA/cm^2)	FF	PCE (%)
C_3N_5	1.065	22.870	0.685	16.686
g-C_3N_4	1.030	21.573	0.691	15.344
Bare	1.040	20.344	0.660	13.959

Figure 12. (a) Current-voltage characteristics of perovskite solar cells made with bare PbX_2, 4 wt% of g-C_3N_4 and C_3N_5 under AM1.5 G one sun illumination. (b) Mott-Schottky plot of the perovskite solar cells based undoped and g-C_3N_4/C_3N_5-doped perovskite active layers. (c) Recombination resistance of perovskite solar cell based on undoped and doped Perovskite layer with CN and MHP in dark. The corresponding equivalent circuit is shown in insets where Rs is series resistance, C is high-frequency capacitance, R is recombination resistance, and Q is a constant phase element (CPE) with coefficient N. (d-i) Nyquist plots for perovskite solar cells made with bare PbX_2, g-C_3N_4 and C_3N_5 doping under dark condition at 0.0, 0.2, 0.4, 0.6, 0.8 and 1.0 V.

Table 4. Photovoltaic performance of HPSCs made with bare PbX_2, 4 wt% g-C_3N_4 and C_3N_5 in PbX_2 solution under AM1.5 G solar simulated light.

		V_{oc}(V)	J_{sc}(mA/cm^2)	FF	PCE (%)
C_3N_5	Maximum	1.065	22.870	0.685	16.686
	Average	1.026±0.043	22.560±1.039	0.654±0.044	15.142±1.442
g-C_3N_4	Maximum	1.030	21.573	0.691	15.344
	Average	0.984±0.042	21.204±0.565	0.670±0.017	13.981±0.949
Bare	Maximum	1.040	20.344	0.660	13.959
	Average	1.041±0.035	20.394±0.200	0.647±0.020	13.713±0.245

The low band gap and extended π conjugation of C_3N_5 makes it an excellent candidate to harvest solar light to drive visible light induced catalytic reaction. Recently plasmonic materials capable of generating hot electrons, coupled with graphenic materials has shown wide potential in plasmon-exciton co-induced surface catalytic reactions.[79] The plasmon-exciton coupling for co-driven chemical reactions can be measured by surface enhanced Raman spectroscopy (SERS).[80] To probe the viability C_3N_5 for promoting chemical reaction on its surface, the transformation of 4NBT (4-nitrobenzenethiol) to DMAB (4,4'-dimercaptoazobenzene) was chosen as model reaction while silver nanocubes (AgNC)[81] were used as plasmonic material. The comparative SERS spectra of NBT adsorbed on bare AgNC, and AgNC decorated on g-C_3N_4 mW and C_3N_5 using 532 nm laser and 1 mW laser power are presented in Figure 13a. Normal Raman spectra of the pristine 4NBT powder show three main Raman signals at 1101, 1332 and 1576 cm^{-1} assigned to S-C stretch, NO_2 vibration and C=C stretch respectively.[82] After irradiating with 532 nm laser with a 1 mW power intensity the N-O vibration was decreased and new peaks at 1142 (C-N stretch), 1389 and 1438 (N=N stretch) cm^{-1} corresponded to DMAB a_g modes emerged demonstrating conversion of 4NBT to DMAB.[83] For bare AgNC the drop in 4NBT peak was not significant which show inefficient surface-plasmon-to-hot-electron conversion to promote plasmon-driven chemical reaction. The AgNC/g-C_3N_4 show a slight lowering of 4NBT peak intensity and rise in DMAB peaks, however, the peak was not disappeared suggesting incomplete transformation at lower laser power. While for AgNC/C_3N_5 the N-O vibration peak was completely disappeared at 1.0 mW laser power. Further, we have tested laser power dependent SERS spectra on NBT adsorbed samples which demonstrate complete disappearance of 4NBT peaks for Ag/C_3N_5 even at 0.7 mW while bare Ag and AgNC/g-C_3N_4 system could not achieve complete degradation even at 10 mW laser power (Figure 13 b-d). Magnified SERS spectra of Ag/C_3N_5, in 1270-1470 cm^{-1} region show a gradual decrease in N-O vibration peak as a function of laser power AgNC and completely disappear at 1.0 mW (Figure S20). While sluggish transformation rate was observed for AgNC/g-C_3N_4 and AgNC as evident from the increase in 4NBT peak at 1332 cm^{-1} along with DMAB peak at 1389 and 1438 cm^{-1} as a function of laser intensity. The excellent conversion efficiency of AgNC/C_3N_5 assembly was attributed due to better plasmon-to-electron conversion efficiency on conjugated C_3N_5's surface which lead to high-density hot electrons to facilitate high catalytic conversion.[79b]

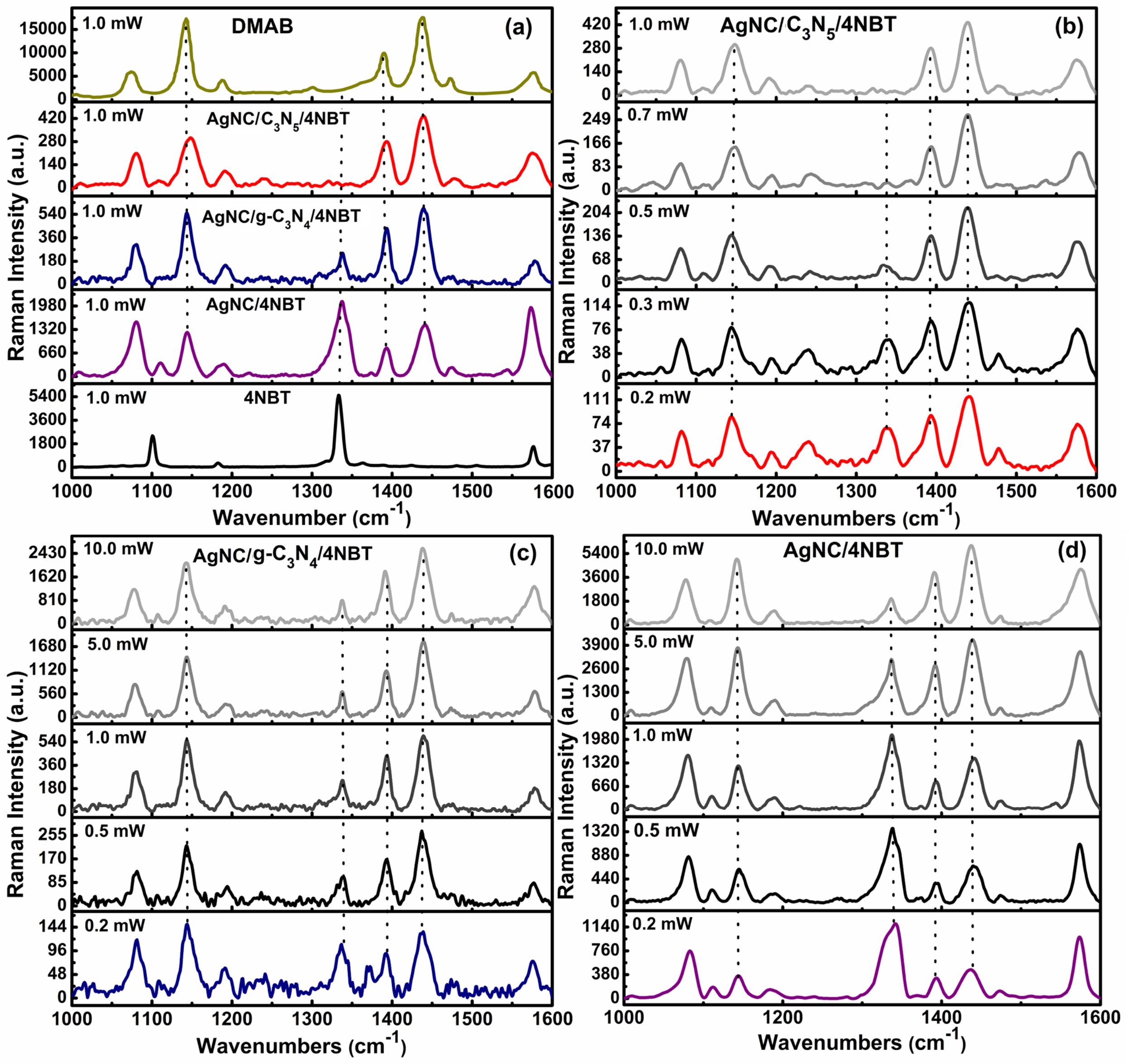

Figure 13. (a) Raman spectrum of pristine 4NBT (black), DMAB (yellow) and comparison of SERS spectra of plasmon-exciton co-induced surface catalytic reaction of 4NBT to DMAB on AgNC (purple), AgNC/g-C_3N_4 (blue) and AgNC/C_3N_5 (red) under 532 nm laser irradiation at 1.0 mW power and 60 s accumulation time and SERS spectra as function of laser power for plasmon-exciton co-induced surface catalytic transformation of 4NBT to DMAB on (b) AgNC/C_3N_5 (c) AgNC/g-C_3N_4 and (d) AgNC. The gradual lightening of color as a function of laser power represents the transformation of 4NBT to DMAB.

We performed thermogravimetric analysis (TGA) analysis of g-C_3N_4 samples to determine the thermal stability of materials (Figure S21). The TGA thermogram of g-C_3N_4 shows two weight loss regimes in the range of 60-150 ºC and 500-740 ºC (Figure S21a). The first small weight loss (~ 6%) in the range of 60-150 ºC was due to loss of surface adsorbed water molecules. The second major weight loss started from 550 ºC, shows slow weight loss (~8%) up to 635 ºC due to loss of NH_2 and condensation of heptazine units followed by almost ~70% sharp weight loss in the range of 635-740 ºC due to degradation of heptazine moieties.[84] Following that, a steady weight loss was observed up to 900 ºC due to the removal of residual carbon material. For C_3N_5, an initial small weight loss of 6% in the range of 60-150 ºC was attributed due to loss of surface adsorbed and intercalated water (Figure S21b). A second steady weight loss (~34%) observed in the temperature range of 420-630 ºC was assigned to loss of bridging azo nitrogens (-N=N-) and edge decorated -NH_2 nitrogens. The absence of any sharp weight loss for azo nitrogens demonstrates that azo nitrogens were not localized but present in a crosslinked heptazine network. Previous reports on azo linked polymer also demonstrated excellent thermal stability of such polymers due to the formation of a rigid structure.[85] Further, the observed weight loss value was in close agreement with expected weight loss value for azo nitrogen (33.5%) calculated by considering removal of three azo nitrogens (-N=N- shared by two heptazine) from azo bridged C_6N_{10} unit, leaving behind C_6N_7 heptazine unit. These results further validated the presence of azo nitrogens in C_3N_5 polymer. Approximately 38% sharp weight loss in 630-720 ºC region was assigned to degradation of heptazine ring system followed by slow weight loss up to 900 ºC for residual carbon. Further, to investigate the nature of the product formed at high temperature, we annealed the sample in a closed evacuated quartz tube at 800 ºC for 4 h. The orange product turned black and stuck to the wall of the tubes. Raman analysis of the product showed specific D, G band along with the 2D band and demonstrate its transformation into N doped graphene/carbon (Figure S22). Previous reports also demonstrate the transformation of carbon nitride-based materials/nitrogenous precursors into N-graphene/N-carbon at higher temperatures.

To understand charge carrier dynamics and recombination mechanisms in C_3N_5, the surface potential changes of the samples under dark and under laser illumination at different wavelengths, were measured using Kelvin Probe Force Microscopy (KPFM) as illustrated in Figure 14. The surface topographical AFM image of g-C_3N_4 and C_3N_5 thin films deposited on bare FTO reveals an average roughness of 20.4 and 19 nm respectively (Figure 14ai and bi). Figure 14(aii)-(av) and (bii)-(bv) displays the surface potential map of g-C_3N_4 and C_3N_5 samples under dark, 635, 520 and 450 nm respectively. The FTO was grounded and behaves as an electron sink for photogenerated charges, leaving holes behind. The surface potential map under dark for both g-C_3N_4 and C_3N_5 shows even distribution of charge all over the surface of samples, (Figure 14(aii) and (bii)). After illumination with 635 nm laser the contrast of blue spots (positive potential shift) in the surface potential map was increased for both g-C_3N_4 and C_3N_5, however, this change was much intense for C_3N_5. Under 520 nm light, the density of blue spots was slightly higher for g-C_3N_4 than C_3N_5 which drastically increased under 450 nm illumination (Figure 14a (aiv)-av) and Figure 14b (biv)-(bv). These observations demonstrate that highest charge generation and accumulation on the surface was at 450 nm for g-C_3N_4 and at 635 nm for C_3N_5 while remaining moderate for both at 520 nm. Further, values of surface potential measured by KPFM under dark condition were found to be +156 and +45 mV for g-C_3N_4 and C_3N_5 respectively, which agreed well with the increased electron density on C_3N_5 than g-C_3N_4 due to contribution of charge from azo motif to heptazine ring system *via* extended orbital overlap (Figure 14c and d). The high surface negative charge of C_3N_5 was also confirmed by zeta potential measurements (Figure S8). After illumination with 450 nm light, the surface potential was negatively shifted reaching maximum +40 mV for g-C_3N_4 and +25 mV for C_3N_5. Higher change in contact potential difference (CPD) or SP i.e. 102 mV for g-C_3N_4 was observed due to good absorption at 450 nm for generation of electron-hole pairs and accumulation of negative charge on the sample surface. The broad surface potential peaks and significantly larger CPD shift for g-C_3N_4 were attributed possibly due to the longer lifetime (as confirmed by TRPL, Figure 8a) of g-C_3N_4 charge carriers resulting into delayed recombination of accumulated charge. Under 520 nm illumination, the surface potential values for g-C_3N_4 and C_3N_5 were measured to be 123 and 8 mV, while the change in SP was found to be 33 and 37 mV, respectively. For g-C_3N_4, relatively small CPD shifting at 520 nm can be explained due to its limited absorption at 520 nm wavelength generating fewer numbers of excitons, while in C_3N_5 most of the photogenerated charge get recombined due to faster recombination rate. Interestingly, C_3N_5 show unusually high SP shift (77 mV) at 635 nm, while g-C_3N_4 show explicitly small CPD shift (30 mV). Exceptional high SP shift at 635 nm, demonstrating azo motif playing a certain role in charge carrier generation and stabilization at a longer wavelength. Azo bridged aromatic compounds are well known for their visible light absorption due to the presence of azo chromophore (-N=N-) in conjugation with aromatic units. The $n\rightarrow\pi^*$ transition corresponding to azo nitrogen nonbonding orbital to the π^* orbital of conjugated nitrogens in azo moiety occurs at low energy giving visible light absorption.[86] In C_3N_5 where electron withdrawing heptazine units (C_6H_7) were bridged together with azo bonds, these low energy transition can take place at 635 nm resulting into increase CPD shift at 635 nm. The high surface potential of C_3N_5 at 635 nm validates its potential to generate excitons at longer wavelengths.

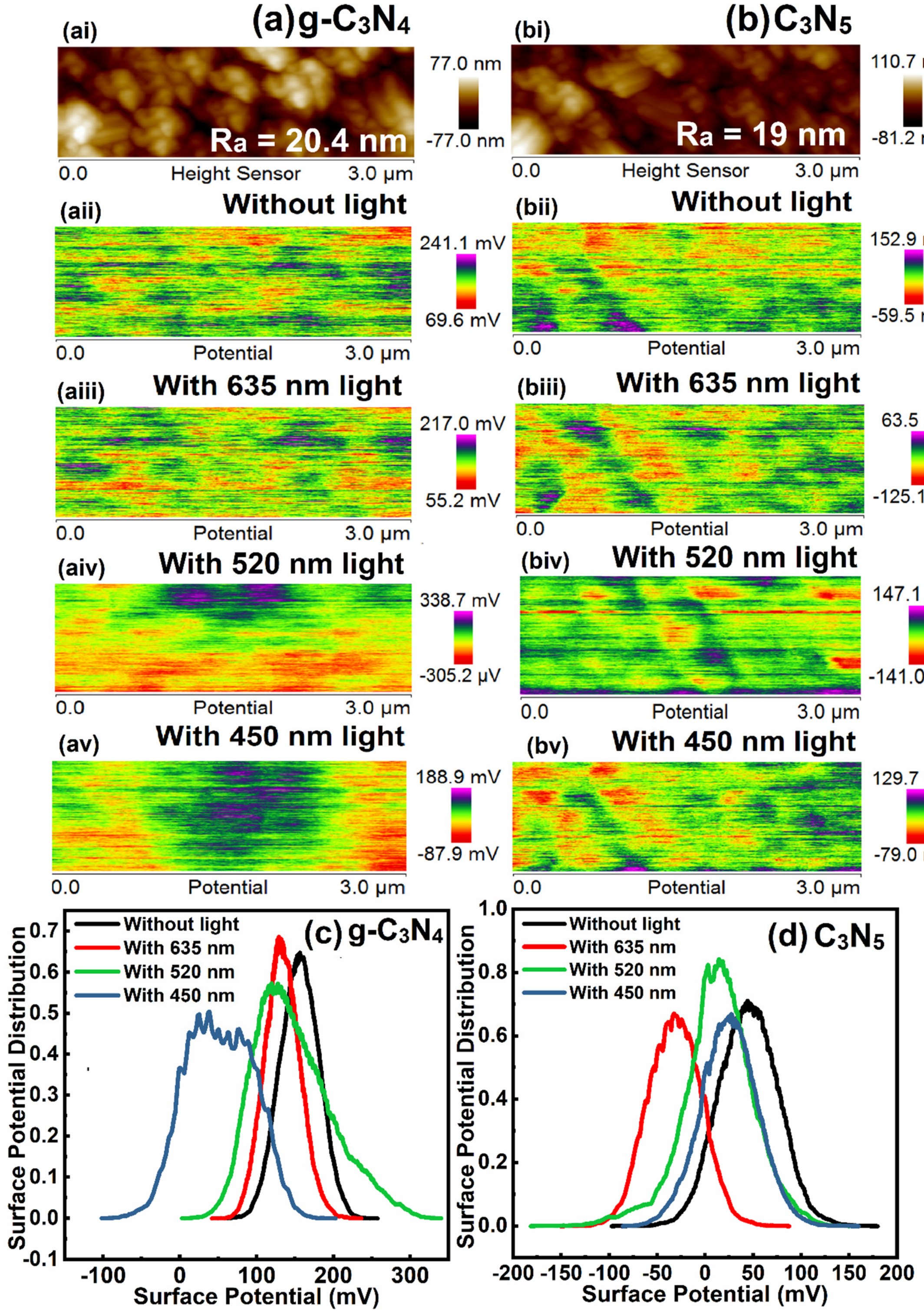
(a) g-C_3N_4
(ai)
R_a = 20.4 nm
77.0 nm
-77.0 nm
0.0
Height Sensor
3.0 µm
(aii)
Without light
241.1 mV
69.6 mV
0.0
Potential
3.0 µm
(aiii)
With 635 nm light
217.0 mV
55.2 mV
0.0
Potential
3.0 µm
(aiv)
With 520 nm light
338.7 mV
-305.2 µV
0.0
Potential
3.0 µm
(av)
With 450 nm light
188.9 mV
-87.9 mV
0.0
Potential
3.0 µm
(b) C_3N_5
(bi)
R_a = 19 nm
110.7 nm
-81.2 nm
0.0
Height Sensor
3.0 µm
(bii)
Without light
152.9 mV
-59.5 mV
0.0
Potential
3.0 µm
(biii)
With 635 nm light
63.5 mV
-125.1 mV
0.0
Potential
3.0 µm
(biv)
With 520 nm light
147.1 mV
-141.0 mV
0.0
Potential
3.0 µm
(bv)
With 450 nm light
129.7 mV
-79.0 mV
0.0
Potential
3.0 µm
(c) g-C_3N_4
Without light
With 635 nm
With 520 nm
With 450 nm
Surface Potential Distribution
-0.1
0.0
0.1
0.2
0.3
0.4
0.5
0.6
0.7
-100
0
100
200
300
Surface Potential (mV)
(d) C_3N_5
Without light
With 635 nm
With 520 nm
With 450 nm
Surface Potential Distribution
0.0
0.2
0.4
0.6
0.8
1.0
-200
-150
-100
-50
0
50
100
150
200
Surface Potential (mV)

Figure 14. (a) and (b) Topographical AFM images (ai), (bi) and Surface potential maps of g-C_3N_4 and C_3N_5 samples deposited on FTO (aii) and (bii) without light, (aiii) and (biii) with 635 nm lased, (aiv) and (biv) with 520 nm laser, (av) and (bv) with 450 nm laser in sequence of top to bottom and surface potential distribution of (c) g-C_3N_4 and (d) C_3N_5 samples deposited on FTO under dark conditions, under illumination with 635, 520 and 450 nm laser.

3. Conclusion

We report the synthesis of a modified carbon nitride framework C_3N_5 polymer containing exceptionally high N:C atomic ratio (5:3) melem hydrazine as the monomeric unit. Extensive characterization of C_3N_5 with XPS, EELS, NMR spectroscopy and elemental analysis suggested the presence of heptazine moiety bridged by azo nitrogens in the C_3N_5 framework. Due to the overlap between the π orbitals of azo-bridged units and the π-conjugated network of the heptazine unit, the bandgap of C_3N_5 material was significantly reduced which, in turn, enabled optical absorption extended up to 700 nm and a bandgap of 1.76 eV. The position of the valence band in C_3N_5 was raised (+1.04 V *vs* NHE) in comparison to g-C_3N_4 (+1.80 V *vs* NHE) and C_3N_5 displayed excellent photosensitizing behavior to sensitize TiO_2 at longer wavelengths (505 nm) to facilitate photoelectrochemical water splitting. Due to the increased nitrogen content and the availability of electron rich basic nitrogen sites, C_3N_5 materials displayed astonishing dye adsorption performance for methylene blue removal reaching 90 % adsorption-desorption equilibria within 1 min and complete adsorption-desorption equilibria within 10 min. In conjunction with Ag nanocubes, C_3N_5 displayed excellent photocatalytic activity for the plasmon-exciton (plexciton) co-driven reduction of 4-nitrobenzenethiol to 4,4'-dimercaptoazobenzene. A prototypical solar cell device using C_3N_5 ETL and $MAPbBr_3$ displayed an improved V_{oc} of 1.3 V and power conversion efficiency (PCE) of 4.2 % higher than g-C_3N_4 ETL. C_3N_5 blended with $MA_xFA_{1-x}Pb(I_{0.85}Br_{0.15})_3$ perovskite active layer achieved a photoconversion efficiency (PCE) as high as 16.7 %.

Supporting Information:

Experimental details; chemical structures; Supporting Figures (Fig. S1-S22); XPS, *ss*NMR, Raman, electrochemical characterization (Mott-Schottky, EIS), PL, Fluorescence lifetime imaging, Zeta potential, EELS, TGA, Photoelectrochemical water splitting results(under AM 1.5G irradiation, LEDs PCE, IPCE, APCE, i-t curve), solar cell results (*J*-*V* curves, action spectra) and plexitonic performance (SERS spectra)

Acknowledgements

We would like to thank the Natural Sciences and Engineering Research Council of Canada (NSERC), the National Research Council Canada (NRC), Future Energy Systems (FES) and CMC Microsystems for direct and indirect (equipment use) financial support. UKT is supported by a graduate student scholarship from Alberta Innovates. Some device fabrication and testing used research infrastructure made possible by a Leaders Opportunity Fund grant to KS from the Canada Foundation for Innovation and the Alberta Small Equipment Grants Program. We acknowledge use of the following facilities: the National Research Council - National Institute for Nanotechnology (NRC-NINT) Electron Microscopy Lab, the Cell Imaging Facility, the Analytical Chemistry Laboratory and the University of Alberta Nanofab. Drs. Shihong Xu and Wayne Moffat are kindly acknowledged for assisting in He-ion imaging, CHNS elemental analysis, respectively. We thank Prof. Alkiviathes Meldrum for allowing the use of his lab to perform PL lifetime measurements.

References

1. (a) Brabec, C. J.; Winder, C.; Sariciftci, N. S.; Hummelen, J. C.; Dhanabalan, A.; van Hal, P. A.; Janssen, R. A. *Adv. Funct. Mater.* **2002,** *12*, 709-712. (b) Kim, J.-S.; Lu, L.; Sreearunothai, P.; Seeley, A.; Yim, K.-H.; Petrozza, A.; Murphy, C. E.; Beljonne, D.; Cornil, J.; Friend, R. H. *J. Am. Chem. Soc.* **2008,** *130*, 13120-13131. (c) Liang, Y. Y.; Yu, L. P. *Acc. Chem. Res.* **2010,** *43*, 1227-1236. (d) Bandara, J.; Shankar, K.; Grimes, C. A.; Thelakkat, M. *Thin Solid Films* **2011,** *520*, 582-590. (e) Baeg, K. J.; Caironi, M.; Noh, Y. Y. *Adv. Mater.* **2013,** *25*, 4210-4244. (f) Hu, X. W.; Dong, Y.; Huang, F.; Gong, X.; Cao, Y. *J. Phys. Chem. C* **2013,** *117*, 6537-6543. (g) Scaccabarozzi, A.; Stingelin, N. *J. Mater. Chem. A* **2014,** *2*, 10818-10824. (h) Fokina, A.; Lee, Y.; Chang, J. H.; Park, M.; Sung, Y.; Bae, W. K.; Char, K.; Lee, C.; Zentel, R. *Adv. Mater. Interfaces* **2016,** *3*, 1600279. (i) Gao, L.; Zhang, Z. G.; Bin, H.; Xue, L.; Yang, Y.; Wang, C.; Liu, F.; Russell, T. P.; Li, Y. *Adv. Mater.* **2016,** *28*, 8288-8295. (j) Mola, G. T.; Dlamini, W. E.; Oseni, S. O. *J. Mater. Sci. Mater. Electron.* **2016,** *27*, 11628-11633. (k) Chang, P.-H.; Tsai, Y.-C.; Shen, S.-W.; Liu, S.-Y.; Huang, K.-Y.; Li, C.-S.; Chang, H.-P.; Wu, C.-I. *ACS Photonics* **2017,** *4*, 2335-2344. (l) Schroeder, B. C.; Kurosawa, T.; Fu, T. R.; Chiu, Y. C.; Mun, J.; Wang, G. J. N.; Gu, X. D.; Shaw, L.; Kneller, J. W. E.; Kreouzis, T.; Toney, M. F.; Bao, Z. A. *Adv. Funct. Mater.* **2017,** *27*, 1701973. (m) Zhao, W.; Li, S.; Zhang, S.; Liu, X.; Hou, J. *Adv. Mater.* **2017,** *29*, 1604059. (n) Kang, M. J.; Khim, D.; Kim, J.; Lee, H. J.; Jo, J. Y.; Baeg, K. J.; Kim, D. Y. *Org. Electron.* **2018,** *58*, 12-17. (o) Brabec, C. J.; Winder, C.; Sariciftci, N. S.; Hummelen, J. C.; Dhanabalan, A.; van Hal, P. A.; Janssen, R. A. J. *Adv. Funct. Mater.* **2002,** *12*, 709-712. (p) Kim, J. S.; Lu, L.; Sreearunothai, P.; Seeley, A.; Yim, K. H.; Petrozza, A.; Murphy, C. E.; Beljonne, D.; Cornil, J.; Friend, R. H. *J. Am. Chem. Soc.* **2008,** *130*, 13120-13131. (q) Bandara, J.; Shankar, K.; Grimes, C. A.; Thelakkat, M. *Thin Solid Films* **2011,** *520*, 582-590. (r) Scaccabarozzi, A. D.; Stingelin, N. *J. Mater. Chem. A* **2014,** *2*, 10818-10824. (s) Gao, L.; Zhang, Z. G.; Bin, H. J.; Xue, L. W.; Yang, Y. K.; Wang, C.; Liu, F.; Russell, T. P.; Li, Y. F. *Adv. Mater.* **2016,** *28*, 8288-8295. (t) Chang, P. H.; Tsai, Y. C.; Shen, S. W.; Liu, S. Y.; Huang, K. Y.; Li, C. S.; Chang, H. P.; Wu, C. I. *ACS Photonics* **2017,** *4*, 2335-2344. (u) Zhong, L.; Gao, L.; Bin, H. J.; Hu, Q.; Zhang, Z. G.; Liu, F.; Russell, T. P.; Zhang, Z. J.; Li, Y. F. *Adv. Energy Mater.* **2017,** *7*, 1602215.

2. Po, R.; Bianchi, G.; Carbonera, C.; Pellegrino, A. *Macromolecules* **2015,** *48*, 453-461.

3. (a) Di Pietro, R.; Fazzi, D.; Kehoe, T. B.; Sirringhaus, H. *J. Am. Chem. Soc.* **2012,** *134*, 14877-14889. (b) Chen, C. Y.; Tsao, C. S.; Huang, Y. C.; Liu, H. W.; Chiu, W. Y.; Chuang, C. M.; Jeng, U. S.; Su, C. J.; Wu, W. R.; Su, W. F.; Wang, L. *Nanoscale* **2013,** *5*, 7629-7638. (c) Phan, H.; Wang, M.; Bazan, G. C.; Nguyen, T. Q. *Adv. Mater.* **2015,** *27*, 7004-7009; (d) Ye, Z.; Cui, H.; Yang, X.; Qiu, F. *J. Mater. Chem. C* **2015,** *3*, 1949-1956. (e) Pearson, A. J.; Hopkinson, P. E.; Couderc, E.; Domanski, K.; Abdi-Jalebi, M.; Greenham, N. C. *Org. Electron.* **2016,** *30*, 225-236. (f) Hsieh, Y. J.; Huang, Y. C.; Liu, W. S.; Su, Y. A.; Tsao, C. S.; Rwei, S. P.; Wang, L. *ACS Appl. Mater. Interfaces* **2017,** *9*, 14808-14816. (g) Un, H. I.; Zheng, Y. Q.; Shi, K.; Wang, J. Y.; Pei, J. *Adv. Funct. Mater.* **2017,** *27*, 1605058. (h) Di Pietro, R.; Fazzi, D.; Kehoe, T. B.; Sirringhaus, H. *J. Am. Chem. Soc.* **2012,** *134*, 14877-14889. (i) Kim, S. H.; Yoon, W. M.; Jang, M.; Yang, H.; Park, J. J.; Park, C. E. *J. Mater. Chem.* **2012,** *22*, 7731-7738. (j) Phan, H.; Wang, M.; Bazan, G. C.; Nguyen, T. Q. *Adv. Mater.* **2015,** *27*, 7004-7004. (k) Ye, Z.; Cui, H. N.; Yang, X. B.; Qiu, F. *J. Mater. Chem. C* **2015,** *3*, 1949-1956. (l) Pearson, A. J.; Hopkinson, P. E.; Couderc, E.; Domanski, K.; Abdi-Jalebi, M.; Greenham, N. C. *Org. Electron.* **2016,** *30*, 225-236. (m) Un, H. I.; Zheng, Y. Q.; Shi, K.; Wang, J. Y.; Pei, J. *Adv. Funct. Mater.* **2017,** *27*, 1605058.

4. (a) Matthews, J. R.; Niu, W. J.; Tandia, A.; Wallace, A. L.; Hu, J. Y.; Lee, W. Y.; Giri, G.; Mannsfeld, S. C. B.; Xie, Y. T.; Cai, S. C.; Fong, H. H.; Bao, Z. N.; He, M. Q. *Chem. Mater.* **2013,** *25*, 782-789. (b) Marzano, G.; Ciasca, C. V.; Babudri, F.; Bianchi, G.; Pellegrino, A.; Po, R.; Farinola, G. M. *Eur. J. Org. Chem.* **2014,** *2014*, 6583-6614. (c) Bohra, H.; Wang, M. F. *J. Mater. Chem. A* **2017,** *5*, 11550-11571.
5. (a) Zhang, X. M.; Wang, A. Z.; Zhao, M. W. *Carbon* **2015,** *84*, 1-8. (b) Berger, D.; Ratsch, C. *Phys. Rev. B* **2016,** *93*, 235441.
6. (a) Kumar, P.; Boukherroub, R.; Shankar, K. *J. Mater. Chem. A* **2018**, *6*, 12876-12931. (b) Linley, S.; Liu, Y.; Ptacek, C. J.; Blowes, D. W.; Gu, F. X. *ACS Appl. Mater. Interfaces* **2014,** *6*, 4658-4668. (c) Putz, M. V.; Buzatu, D. L.; Mirica, M. C.; Ori, O. *Fuller. Nanotub. Carbon Nanostruct.* **2018,** *26*, 303-314.
7. (a) Sridharan, K.; Kuriakose, T.; Philip, R.; Park, T. J. *Appl. Surf. Sci.* **2014,** *308*, 139-147. (b) Liu, J.; Liu, Y.; Liu, N.; Han, Y.; Zhang, X.; Huang, H.; Lifshitz, Y.; Lee, S.-T.; Zhong, J.; Kang, Z. *Science* **2015,** *347*, 970. (c) Kumar, P.; Thakur, U. K.; Alam, K.; Kar, P.; Kisslinger, R.; Zeng, S.; Patel, S.; Shankar, K. *Carbon* **2018,** *137*, 174-187.
8. Wen, J.; Xie, J.; Chen, X.; Li, X. *Appl. Surf. Sci.* **2017,** *391*, 72-123.
9. (a) Zhou, Z.; Zhang, Y.; Shen, Y.; Liu, S.; Zhang, Y. *Chem. Soc. Rev.* **2018,** *47*, 2298-2321. (b) Ong, W.-J.; Tan, L.-L.; Ng, Y. H.; Yong, S.-T.; Chai, S.-P. *Chem. Rev.* **2016,** *116*, 7159-7329. (c) Zheng, Y.; Lin, L.; Wang, B.; Wang, X. *Angew. Chem. Int. Ed.* **2015,** *54*, 12868-12884.
10. (a) Cao, S.; Low, J.; Yu, J.; Jaroniec, M. *Adv. Mater.* **2015,** *27*, 2150-2176. (b) Wang, Y.; Wang, X.; Antonietti, M. *Angew. Chem. Int. Ed.* **2012,** *51*, 68-89. (c) Wang, Y.; Zhang, J.; Wang, X.; Antonietti, M.; Li, H. *Angew. Chem. Int. Ed.* **2010,** *49*, 3356-3359.
11. (a) Zhang, Y.; Mori, T.; Ye, J.; Antonietti, M. *J. Am. Chem. Soc.* **2010,** *132*, 6294-6295. (b) Hong, J.; Xia, X.; Wang, Y.; Xu, R. *J. Mater. Chem.* **2012,** *22*, 15006-15012. (c) Wang, Y.; Di, Y.; Antonietti, M.; Li, H.; Chen, X.; Wang, X. *Chem. Mater.* **2010,** *22*, 5119-5121. (d) Ran, J.; Ma, T. Y.; Gao, G.; Du, X.-W.; Qiao, S. Z. *Energy Environ. Sci.* **2015,** *8*, 3708-3717. (e) Lin, J.; Pan, Z.; Wang, X. *ACS Sustainable Chem. Eng.* **2013,** *2*, 353-358. (f) Wang, Y.; Li, H.; Yao, J.; Wang, X.; Antonietti, M. *Chem. Sci.* **2011,** *2*, 446-450.
12. (a) Yang, S.; Gong, Y.; Zhang, J.; Zhan, L.; Ma, L.; Fang, Z.; Vajtai, R.; Wang, X.; Ajayan, P. M. *Adv. Mater.* **2013,** *25*, 2452-2456. (b) Kumar, A.; Kumar, P.; Joshi, C.; Ponnada, S.; Pathak, A. K.; Ali, A.; Sreedhar, B.; Jain, S. L. *Green Chem.* **2016,** *18*, 2514-2521. (c) Kumar, A.; Kumar, P.; Pathak, A. K.; Chokkapu, A. N.; Jain, S. L. *ChemistrySelect* **2017,** *2*, 3437-3443.
13. Mane, G. P.; Talapaneni, S. N.; Lakhi, K. S.; Ilbeygi, H.; Ravon, U.; Al-Bahily, K.; Mori, T.; Park, D. H.; Vinu, A. *Angew. Chem. Int. Ed.* **2017,** *56*, 8481-8485.
14. (a) Mane, G. P.; Dhawale, D. S.; Anand, C.; Ariga, K.; Ji, Q.; Wahab, M. A.; Mori, T.; Vinu, A. *J. Mater. Chem. A* **2013,** *1*, 2913-2920. (b) Talapaneni, S. N.; Mane, G. P.; Park, D.-H.; Lakhi, K. S.; Ramadass, K.; Joseph, S.; Skinner, W. M.; Ravon, U.; Al-Bahily, K.; Vinu, A. *J. Mater. Chem. A* **2017,** *5*, 18183-18192. (c) Talapaneni, S. N.; Mane, G. P.; Mano, A.; Anand, C.; Dhawale, D. S.; Mori, T.; Vinu, A. *ChemSusChem* **2012,** *5*, 700-708. (d) Lakhi, K. S.; Park, D.-H.; Al-Bahily, K.; Cha, W.; Viswanathan, B.; Choy, J.-H.; Vinu, A. *Chem. Soc. Rev.* **2017,** *46*, 72-101.
15. Kim, I. Y.; Kim, S.; Jin, X.; Premkumar, S.; Chandra, G.; Lee, N.-S.; Mane, G. P.; Hwang, S.-J.; Umapathy, S.; Vinu, A. *Angew. Chem.* **2018,** *130*, 17381-17386.
16. Fang, J.; Fan, H.; Li, M.; Long, C. *J. Mater. Chem. A* **2015,** *3*, 13819-13826.
17. Zhang, P.; Li, X.; Shao, C.; Liu, Y. *J. Mater. Chem. A* **2015,** *3*, 3281-3284.

18. (a) Jürgens, B.; Irran, E.; Senker, J.; Kroll, P.; Müller, H.; Schnick, W. *J. Am. Chem. Soc.* **2003,** *125*, 10288-10300. (b) Chu, S.; Wang, C.; Feng, J.; Wang, Y.; Zou, Z. *Int. J. Hydrog. Energy* **2014,** *39*, 13519-13526. (c) Saplinova, T.; Lehnert, C.; Böhme, U.; Wagler, J.; Kroke, E. *New J. Chem.* **2010,** *34*, 1893-1908. (d) Chu, S.; Wang, Y.; Guo, Y.; Feng, J.; Wang, C.; Luo, W.; Fan, X.; Zou, Z. *ACS Catal.* **2013,** *3*, 912-919.
19. Shiraishi, Y.; Kanazawa, S.; Kofuji, Y.; Sakamoto, H.; Ichikawa, S.; Tanaka, S.; Hirai, T. *Angew. Chem. Int. Ed.* **2014,** *53*, 13454-13459.
20. Che, W.; Cheng, W.; Yao, T.; Tang, F.; Liu, W.; Su, H.; Huang, Y.; Liu, Q.; Liu, J.; Hu, F. *J. Am. Chem. Soc.* **2017,** *139*, 3021-3026.
21. (a) Miller, D. R.; Swenson, D. C.; Gillan, E. G. *J. Am. Chem. Soc.* **2004,** *126*, 5372-5373. (b) Miller, D. R.; Holst, J. R.; Gillan, E. G. *Inorg. Chem.* **2007,** *46*, 2767-2774.
22. Gillan, E. G. *Chem. Mater.* **2000,** *12*, 3906-3912.
23. (a) Saplinova, T.; Bakumov, V.; Gmeiner, T.; Wagler, J.; Schwarz, M.; Kroke, E. *Z. Anorg. Allg. Chem.* **2009,** *635*, 2480-2487. (b) Sattler, A.; Schönberger, S.; Schnick, W. *Z. Anorg. Allg. Chem.* **2010,** *636*, 476-482.
24. Makowski, S. J.; Köstler, P.; Schnick, W. *Chem. Eur. J.* **2012,** *18*, 3248-3257.
25. (a) Kumar, A.; Kumar, P.; Borkar, R.; Bansiwal, A.; Labhsetwar, N.; Jain, S. L. *Carbon* **2017,** *123*, 371-379. (b) Yu, H.; Shi, R.; Zhao, Y.; Bian, T.; Zhao, Y.; Zhou, C.; Waterhouse, G. I.; Wu, L. Z.; Tung, C. H.; Zhang, T. *Adv. Mater.* **2017,** *29*, 1605148.
26. (a) Xia, P.; Zhu, B.; Yu, J.; Cao, S.; Jaroniec, M. *J. Mater. Chem. A* **2017,** *5*, 3230-3238. (b) Mao, J.; Peng, T.; Zhang, X.; Li, K.; Ye, L.; Zan, L. *Catal. Sci. Technol.* **2013,** *3*, 1253-1260.
27. Axen, N.; Botton, G.; Somekh, R.; Hutchings, I. *Diam. Relat. Mater.* **1996,** *5*, 163-168.
28. Hu, J.; Yang, P.; Lieber, C. M. *Phys. Rev. B* **1998,** *57*, R3185.
29. Li, X.; Zhang, J.; Shen, L.; Ma, Y.; Lei, W.; Cui, Q.; Zou, G. *Appl. Phys. A* **2009,** *94*, 387-392.
30. Seyfarth, L.; Senker, J. *Phys. Chem. Chem. Phys.* **2009,** *11*, 3522-3531.
31. (a) Sehnert, J.; Baerwinkel, K.; Senker, J. *J. Phys. Chem. B* **2007,** *111*, 10671-10680. (b) Hu, Y.; Shim, Y.; Oh, J.; Park, S.; Park, S.; Ishii, Y. *Chem. Mater.* **2017,** *29*, 5080-5089.
32. Cui, Y.; Ding, Z.; Fu, X.; Wang, X. *Angew. Chem. Int. Ed.* **2012,** *51*, 11814-11818.
33. Sattler, A.; Pagano, S.; Zeuner, M.; Zurawski, A.; Gunzelmann, D.; Senker, J.; Müller-Buschbaum, K.; Schnick, W. *Chem. Eur. J.* **2009,** *15*, 13161-13170.
34. (a) Hsu, C.-Y.; Chang, K.-S. *J.Phys. Chem. C* **2018,** *122*, 3506-3512. (b) Rovnyak, D.; Baldus, M.; Itin, B. A.; Bennati, M.; Stevens, A.; Griffin, R. G. *J. Phys. Chem. B* **2000,** *104*, 9817-9822.
35. Lotsch, B. V.; Schnick, W. *Chem. Eur. J.* **2007,** *13*, 4956-4968.
36. Guo, Q.; Zhang, Y.; Qiu, J.; Dong, G. *J. Mater. Chem. C* **2016,** *4*, 6839-6847.
37. (a) Gulaczyk, I.; Kręglewski, M.; Valentin, A. *J. Mol. Spectrosc.* **2003,** *220*, 132-136. (b) Dirtu, D.; Odochian, L.; Pui, A.; Humelnicu, I. *Open Chem.* **2006,** *4*, 666-673.
38. (a) Niu, P.; Zhang, L.; Liu, G.; Cheng, H. M. *Adv. Funct. Mater.* **2012,** *22*, 4763-4770; (b) Xu, J.; Zhang, L.; Shi, R.; Zhu, Y. *J. Mater. Chem. A* **2013,** *1*, 14766-14772.
39. (a) Zheng, H.; Chen, W.; Gao, H.; Wang, Y.; Guo, H.; Guo, S.; Tang, Z.; Zhang, J. *J. Mater. Chem. C* **2017,** *5*, 10746-10753. (b) Lau, V. W.-h.; Mesch, M. B.; Duppel, V.; Blum, V.; Senker, J. r.; Lotsch, B. V. *J. Am. Chem. Soc.* **2015,** *137*, 1064-1072.
40. (a) Wang, X.; Maeda, K.; Thomas, A.; Takanabe, K.; Xin, G.; Carlsson, J. M.; Domen, K.; Antonietti, M. *Nat. Mater.* **2009,** *8*, 76. (b) Bojdys, M. J.; Müller, J. O.; Antonietti, M.; Thomas, A. *Chem. Eur. J.* **2008,** *14*, 8177-8182.

41. Kroke, E.; Schwarz, M.; Horath-Bordon, E.; Kroll, P.; Noll, B.; Norman, A. D. *New J. Chem.* **2002,** *26*, 508-512.
42. Tonda, S.; Kumar, S.; Kandula, S.; Shanker, V. *J. Mater. Chem. A* **2014,** *2*, 6772-6780.
43. Jiang, J.; Ou-yang, L.; Zhu, L.; Zheng, A.; Zou, J.; Yi, X.; Tang, H. *Carbon* **2014,** *80*, 213-221.
44. Cui, Y.; Zhang, J.; Zhang, G.; Huang, J.; Liu, P.; Antonietti, M.; Wang, X. *J. Mater. Chem.* **2011,** *21*, 13032-13039.
45. Zhang, J.; Zhang, M.; Lin, S.; Fu, X.; Wang, X. *J. Catal.* **2014,** *310*, 24-30.
46. (a) Sharma, P.; Sasson, Y. *Green Chem.* **2017,** *19*, 844-852. (b) Yuan, B.; Chu, Z.; Li, G.; Jiang, Z.; Hu, T.; Wang, Q.; Wang, C. *J. Mater. Chem. C* **2014,** *2*, 8212-8215.
47. Zhang, G.; Zhang, M.; Ye, X.; Qiu, X.; Lin, S.; Wang, X. *Adv. Mater.* **2014,** *26*, 805-809.
48. (a) Shalom, M.; Inal, S.; Fettkenhauer, C.; Neher, D.; Antonietti, M. *J. Am. Chem. Soc.* **2013,** *135*, 7118-7121. (b) Shalom, M.; Guttentag, M.; Fettkenhauer, C.; Inal, S.; Neher, D.; Llobet, A.; Antonietti, M. *Chem. Mater.* **2014,** *26*, 5812-5818.
49. (a) Kang, Y.; Yang, Y.; Yin, L. C.; Kang, X.; Wang, L.; Liu, G.; Cheng, H. M. *Adv. Mater.* **2016,** *28*, 6471-6477. (b) Yang, P.; Ou, H.; Fang, Y.; Wang, X. *Angew. Chem. Int. Ed.* **2017,** *56*, 3992-3996.
50. Alibart, F.; Lejeune, M.; Durand Drouhin, O.; Zellama, K.; Benlahsen, M. *J. Appl. Phys.* **2010,** *108*, 053504.
51. (a) Zhang, Y.; Pan, Q.; Chai, G.; Liang, M.; Dong, G.; Zhang, Q.; Qiu, J. *Sci. Rep.* **2013,** *3*, 1943. (b) Sun, C.; Tay, B.; Lau, S.; Sun, X.; Zeng, X.; Li, S.; Bai, H.; Liu, H.; Liu, Z.; Jiang, E. *J. Appl. Phys.* **2001,** *90*, 2615-2617.
52. Niu, P.; Liu, G.; Cheng, H.-M. *J. Phys. Chem. C* **2012,** *116*, 11013-11018.
53. (a) Chen, L. C.; Teng, C. Y.; Lin, C. Y.; Chang, H. Y.; Chen, S. J.; Teng, H. *Adv. Energy Mater.* **2016,** *6*, 1600719. (b) Yeh, T. F.; Teng, C. Y.; Chen, S. J.; Teng, H. *Adv. Mater.* **2014,** *26*, 3297-3303. (c) Yeh, T.-F.; Chen, S.-J.; Yeh, C.-S.; Teng, H. *J. Phys. Chem. C* **2013,** *117*, 6516-6524. (d) Shi, R.; Li, Z.; Yu, H.; Shang, L.; Zhou, C.; Waterhouse, G. I.; Wu, L. Z.; Zhang, T. *ChemSusChem* **2017,** *10*, 4650-4656. (e) Chen, L. C.; Teng, C. Y.; Lin, C. Y.; Chang, H. Y.; Chen, S. J.; Teng, H. *Adv. Energy Mater.* **2016,** *6*, 1600719. (f) Run, S.; Zi, L.; Huijun, Y.; Lu, S.; Chao, Z.; N., W. G. I.; Li-Zhu, W.; Tierui, Z. *ChemSusChem* **2017,** *10* , 4650-4656.
54. Liang, Q.; Li, Z.; Huang, Z. H.; Kang, F.; Yang, Q. H. *Adv. Funct. Mater.* **2015,** *25*, 6885-6892.
55. (a) Sun, J.; Zhang, J.; Zhang, M.; Antonietti, M.; Fu, X.; Wang, X. *Nat. Commun.* **2012,** *3*, 1139. (b) Liu, Q.; Chen, T.; Guo, Y.; Zhang, Z.; Fang, X. *Appl. Catal. B.* **2016,** *193*, 248-258. (c) Ye, X.; Cui, Y.; Wang, X. *ChemSusChem* **2014,** *7*, 738-742.
56. (a) Chen, Z.; Sun, P.; Fan, B.; Liu, Q.; Zhang, Z.; Fang, X. *Appl. Catal. B* **2015,** *170*, 10-16. (b) Zhang, M.; Duan, Y.; Jia, H.; Wang, F.; Wang, L.; Su, Z.; Wang, C. *Catal. Sci. Technol.* **2017,** *7*, 452-458.
57. (a) Qin, J.; Wang, S.; Ren, H.; Hou, Y.; Wang, X. *Appl. Catal. B* **2015,** *179*, 1-8. (b) Luo, L.; Zhang, M.; Wang, P.; Wang, Y.; Wang, F. *New J. Chem.* **2018,** *42*, 1087-1091.
58. Ali, H. *Water Air Soil Pollution* **2010,** *213*, 251-273.
59. Mittal, A.; Mittal, J.; Malviya, A.; Kaur, D.; Gupta, V. *J. Colloid Interface Sci.* **2010,** *343*, 463-473.
60. Yagub, M. T.; Sen, T. K.; Afroze, S.; Ang, H. M. *Adv. Colloid Interface Sci.* **2014,** *209*, 172-184.

61. (a) Fronczak, M.; Krajewska, M.; Demby, K.; Bystrzejewski, M. *J. Phys. Chem. C* **2017,** *121*, 15756-15766. (b) Zhu, B.; Xia, P.; Ho, W.; Yu, J. *Appl. Surf. Sci.* **2015,** *344*, 188-195.
62. Langmuir, I. *J. Am. Chem. Soc.* **1918,** *40*, 1361-1403.
63. Freundlich, H. *J. Phys. Chem.* **1906,** *57*, 1100-1107.
64. Han, S.; Liu, K.; Hu, L.; Teng, F.; Yu, P.; Zhu, Y. *Sci. Rep.* **2017,** *7*, 43599.
65. Gaya, U. I.; Abdullah, A. H. *J. Photochem. Photobiol. C Photochem. Rev.* **2008,** *9*, 1-12.
66. Ahmad, H.; Kamarudin, S.; Minggu, L.; Kassim, M. *Renew. Sustainable Energy Rev.* **2015,** *43*, 599-610.
67. Pelaez, M.; Nolan, N. T.; Pillai, S. C.; Seery, M. K.; Falaras, P.; Kontos, A. G.; Dunlop, P. S.; Hamilton, J. W.; Byrne, J. A.; O'shea, K. *Appl. Catal. B* **2012,** *125*, 331-349.
68. Zhou, X.; Peng, F.; Wang, H.; Yu, H.; Fang, Y. *Chem. Commun.* **2011,** *47*, 10323-10325.
69. (a) Zheng, X. J.; Chen, B.; Yang, M. J.; Wu, C. C.; Orler, B.; Moore, R. B.; Zhu, K.; Priya, S. *ACS Energy Lett.* **2016,** *1*, 424-430. (b) Askar, A. M.; Bernard, G. M.; Wiltshire, B.; Shankar, K.; Michaelis, V. K. *J. Phys. Chem. C* **2017,** *121*, 1013-1024.
70. Zhao, Y.; Nardes, A. M.; Zhu, K. *Faraday Discuss.* **2014,** *176*, 301-312.
71. Wu, C. G.; Chiang, C. H.; Chang, S. H. *Nanoscale* **2016,** *8*, 4077-4085.
72. Li, Z.; Boix, P. P.; Xing, G. C.; Fu, K. W.; Kulkarni, S. A.; Batabyal, S. K.; Xu, W. J.; Cao, A. Y.; Sum, T. C.; Mathews, N.; Wong, L. H. *Nanoscale* **2016,** *8*, 6352-6360.
73. Zuo, C. T.; Ding, L. M. *Adv. Energy Mater.* **2017,** *7*, 1601193.
74. Liang, Y. Q.; Wang, Y. J.; Mu, C.; Wang, S.; Wang, X. N.; Xu, D. S.; Sun, L. C. *Adv. Energy Mater.* **2018,** *8*, 1701159.
75. Sheng, R.; Ho-Baillie, A.; Huang, S. J.; Chen, S.; Wen, X. M.; Hao, X. J.; Green, M. A. *J. Phys. Chem. C* **2015,** *119*, 3545-3549.
76. Ryu, S.; Noh, J. H.; Jeon, N. J.; Kim, Y. C.; Yang, S.; Seo, J. W.; Seok, S. I. *Energy Environ. Sci.* **2014,** *7*, 2614-2618.
77. (a) Chen, X.; Liu, Q.; Wu, Q.; Du, P.; Zhu, J.; Dai, S.; Yang, S. *Adv. Funct. Mater.* **2016,** *26*, 1719-1728. (b) He, M.; Chen, Y.; Liu, H.; Wang, J.; Fang, X.; Liang, Z. *Chem. Commun.* **2015,** *51*, 9659-9661. (c) Zhu, Z.; Ma, J.; Wang, Z.; Mu, C.; Fan, Z.; Du, L.; Bai, Y.; Fan, L.; Yan, H.; Phillips, D. L. *J. Am. Chem. Soc.* **2014,** *136*, 3760-3763. (d) Hadadian, M.; Correa-Baena, J. P.; Goharshadi, E. K.; Ummadisingu, A.; Seo, J. Y.; Luo, J.; Gholipour, S.; Zakeeruddin, S. M.; Saliba, M.; Abate, A. *Adv. Mater.* **2016,** *28*, 8681-8686. (e) Jiang, L. L.; Wang, Z. K.; Li, M.; Zhang, C. C.; Ye, Q. Q.; Hu, K. H.; Lu, D. Z.; Fang, P. F.; Liao, L. S. *Adv. Funct. Mater.* **2018,** *28*, 1705875.
78. (a) Kirchartz, T.; Gong, W.; Hawks, S. A.; Agostinelli, T.; MacKenzie, R. C. I.; Yang, Y.; Nelson, J. *J. Phys. Chem. C* **2012,** *116*, 7672-7680. (b) Guo, X.; Tan, Q.; Liu, S.; Qin, D.; Mo, Y.; Hou, L.; Liu, A.; Wu, H.; Ma, Y. *Nano Energy* **2018,** *46*, 150-157. (c) Liu, Z.; Zhu, A.; Cai, F.; Tao, L.; Zhou, Y.; Zhao, Z.; Chen, Q.; Cheng, Y.-B.; Zhou, H. *J. Mater. Chem. A* **2017,** *5*, 6597-6605. (d) Liu, Z.; Chang, J.; Lin, Z.; Zhou, L.; Yang, Z.; Chen, D.; Zhang, C.; Liu, S.; Hao, Y. *Adv. Energy Mater.* **2018,** *8*, 1703432. (e) Jahandar, M.; Heo, J. H.; Song, C. E.; Kong, K.-J.; Shin, W. S.; Lee, J.-C.; Im, S. H.; Moon, S.-J. *Nano Energy* **2016,** *27*, 330-339. (f) He, Q.; Yao, K.; Wang, X.; Xia, X.; Leng, S.; Li, F. *ACS Appl. Mater. Interfaces* **2017,** *9*, 41887-41897. (g) Niu, G.; Wang, S.; Li, J.; Li, W.; Wang, L. *J. Mater. Chem. A* **2018,** *6*, 4721-4728.
79. (a) Lin, W.; Cao, E.; Zhang, L.; Xu, X.; Song, Y.; Liang, W.; Sun, M. *Nanoscale* **2018,** *10*, 5482-5488. (b) Kang, L.; Chu, J.; Zhao, H.; Xu, P.; Sun, M. *J. Mater. Chem. C* **2015,** *3*, 9024-9037. (c) Ding, Q.; Shi, Y.; Chen, M.; Li, H.; Yang, X.; Qu, Y.; Liang, W.; Sun, M. *Sci. Rep.* **2016,**

6, 32724. (d) Wu, H. Y.; Lai, Y. H.; Hsieh, M. S.; Lin, S. D.; Li, Y. C.; Lin, T. W. *Adv. Mater. Interfaces* **2014,** *1*, 1400119.
80. (a) Liang, X.; You, T.; Liu, D.; Lang, X.; Tan, E.; Shi, J.; Yin, P.; Guo, L. *Phys. Chem. Chem. Phys.* **2015,** *17*, 10176-10181. (b) Zhao, J.; Sun, M.; Liu, Z.; Quan, B.; Gu, C.; Li, J. *Sci. Rep.* **2015,** *5*, 16019.
81. Siekkinen, A. R.; McLellan, J. M.; Chen, J.; Xia, Y. *Chem. Phys. lett.* **2006,** *432*, 491-496.
82. Dong, B.; Fang, Y.; Xia, L.; Xu, H.; Sun, M. *J. Raman Spectrosc.* **2011,** *42*, 1205-1206.
83. (a) Canpean, V.; Iosin, M.; Astilean, S. *Chem. Phys. Lett.* **2010,** *500*, 277-282. (b) Fang, Y.; Li, Y.; Xu, H.; Sun, M. *Langmuir* **2010,** *26*, 7737-7746.
84. (a) Kang, Y.; Yang, Y.; Yin, L. C.; Kang, X.; Liu, G.; Cheng, H. M. *Adv. Mater.* **2015,** *27*, 4572-4577. (b) Niu, P.; Qiao, M.; Li, Y.; Huang, L.; Zhai, T. *Nano Energy* **2018,** *44*, 73-81.
85. (a) Dang, Q.-Q.; Wang, X.-M.; Zhan, Y.-F.; Zhang, X.-M. *Polym. Chem.* **2016,** *7*, 643-647. (b) Patel, H. A.; Je, S. H.; Park, J.; Chen, D. P.; Jung, Y.; Yavuz, C. T.; Coskun, A. *Nat. Commun.* **2013,** *4*, 1357. (c) Patel, H. A.; Je, S. H.; Park, J.; Jung, Y.; Coskun, A.; Yavuz, C. T. *Chem. Eur. J.* **2014,** *20*, 772-780.
86. (a) Clark, M., *Handbook of textile and industrial dyeing: principles, processes and types of dyes*. Elsevier: 2011. (b) Zollinger, H. *Color chemistry: syntheses, properties, and applications of organic dyes and pigments*. John Wiley & Sons: 2003. (c) Robin, M. B.; Simpson, W. T. *J. Chem. Phys.* **1962,** *36*, 580-588.

Graphical abstract